Scanning Tunneling Microscopy Study and Nanomanipulation of Graphene-Coated Water on Mica

Kevin T. He,[†,§,⊥] Joshua D. Wood,[†,‡,§,⊥] Gregory P. Doidge,[†,‡,§] Eric Pop,[†,‡,§] and Joseph W. Lyding*[,†,§]

[†]Department of Electrical and Computer Engineering, [‡]Micro and Nanotechnology Lab, and [§]Beckman Institute for Advanced Science and Technology, University of Illinois at Urbana−Champaign, Urbana, Illinois 61801, United States

S *Supporting Information*

ABSTRACT: We study interfacial water trapped between a sheet of graphene and a muscovite (mica) surface using Raman spectroscopy and ultrahigh vacuum scanning tunneling microscopy (UHV-STM) at room temperature. We are able to image the graphene−water interface with atomic resolution, revealing a layered network of water trapped underneath the graphene. We identify water layer numbers with a carbon nanotube height reference. Under normal scanning conditions, the water structures remain stable. However, at greater electron energies, we are able to locally manipulate the water using the STM tip.

KEYWORDS: *Graphene, water, mica, scanning probe microscopy, atomic resolution, STM, Raman*
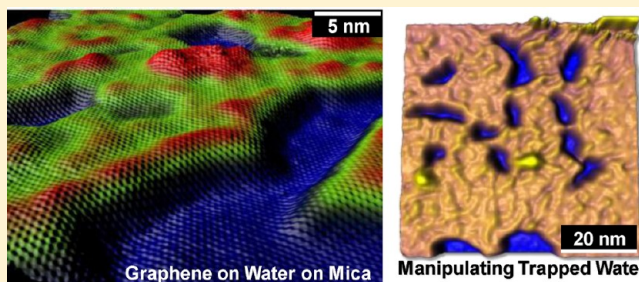
The interface between water and various surfaces[1,2] at room temperature has been of great interest to scientists due to its relevance in geology,[3] biology,[4] and, most recently, electronics.[5,6] It has been demonstrated that water behaves very differently at an interface than it does in the bulk state, forming semiordered "hydration layers" close to the solid surface.[7−10] However, the exact nature of these hydration layers is still not well understood and remains the source of much controversy.[11] Recent studies utilizing AFM and other methods have made progress toward putting some of these controversies to rest,[6,11−14] but atomic-resolution imaging of the interface had not yet been achieved.

Graphene[6,15−20] has already been extensively characterized by surface imaging techniques on a variety of substrates,[21−26] but only recently has it started to see use as a template for studying other substances.[13,27,28] Graphene is ideal for coating and trapping volatile molecules for both scanning probe microscopy[13,27,29] and electron microscopy[28] studies in that it is conductive, chemically inert, impermeable,[30] and atomically conforms to most substrates.[31] In this Letter, we build upon the work performed by Xu et al.[13] and use the atomic resolution and cleanliness of the ultrahigh vacuum scanning tunneling microscope (UHV-STM) to characterize water confined between monolayer graphene and the mica surface at room temperature. Unlike previous studies of graphene on mica,[6,13,14,27,29,31,32] we use graphene grown on copper via chemical vapor deposition (CVD)[33,34] rather than graphene mechanically exfoliated from graphite.[19] While CVD graphene is inferior to exfoliated graphene in terms of carrier mobility, this drawback is offset by the ability to manufacture large, monolayer sheets and transfer them onto arbitrary substrates.[21,34]

Our CVD process uses a methane-to-hydrogen partial pressure ratio of 2:1 in order to obtain higher monolayer coverage.[35,36] Our previous work[33] and the Supporting Information give more details on our growth procedure. We transfer graphene to mica with poly(methyl methacrylate) (PMMA) and use successive deionized (DI) water baths to clean the graphene films from etchant contamination. The final transfer occurs on a freshly cleaved mica surface within a DI bath, in contrast to previous graphene−water−mica studies.[13,27,29] In this total water immersion, we expect there to be a high amount of water initially trapped under the graphene film. We subject the samples to 60 °C heating for 5 min in air to bring the PMMA−graphene system into intimate contact with the mica, driving out most of the excess water and achieving strong graphene adhesion.[37] Wet transfers had larger area coverage than dry transfers, thereby allowing STM experiments to be conducted. Thus, the water plays a critical role in bringing the graphene and mica into contact, similar to CNT film transfer.[38] After we transfer the graphene onto the water-coated mica and remove the PMMA, we confirm its presence by optical imaging and spectroscopy. After loading into UHV (∼5 × 10^{-11} torr), we degas the samples at ∼650−700 °C for several hours to remove surface adsorbates and contaminants.

Figure 1a gives an optical image of the STM sample with a tear in the monolayer film. Monolayer graphene on transparent mica gives ∼2.3% white light absorbance per layer,[39] assisting in identifying graphene coverage. To determine whether we have trapped water under the graphene, we show high wavenumber
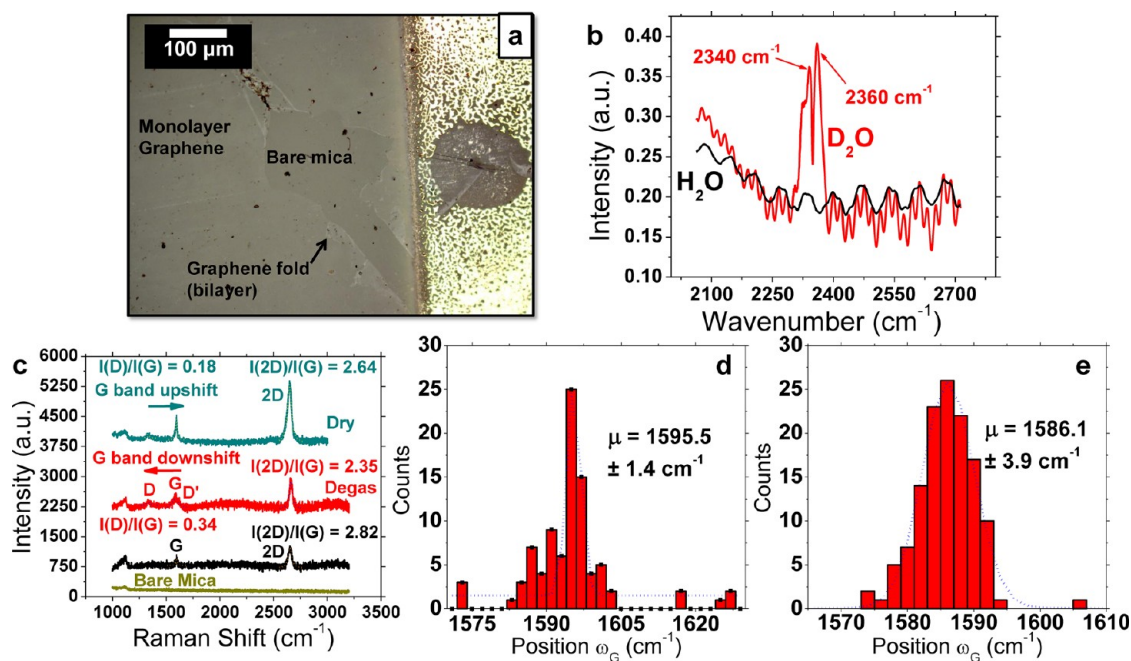
Figure 1. Optical characterization and spectroscopy of graphene-coated water on mica. (a) Optical image of the contacted sample used in STM experiments, showing monolayer graphene, folds in the CVD film, and the bare mica through a tear in the graphene. (b) Fourier transform infrared (FTIR) spectra of graphene transferred to mica in final baths composed of H_2O and D_2O showing a doubly peaked signal for trapped D_2O under graphene. This is contrasts with the trapped H_2O signal, which is simply noise. Both peaks correspond to stretch modes for the O−D bond, confirming the heavy water trapped by graphene. (c) Point Raman spectra (λ_{exc} = 633 nm) of dry transferred monolayer graphene (intensity ratio $I_{2D}/I_G > 2$ from peak fitting) on mica and H_2O-transferred graphene before (black) and after (red) a high temperature degas. The dry transferred graphene's G band position is upshifted to ~1595 cm^{-1}, whereas the degas introduces some defects and downshifts the G band to ~1586 cm^{-1} for trapped few-layer water. Histogram of G band position from Raman mapping before (d) and after (e) the ~650 °C degas. After the degas, the G band's mean position is close to what is expected for graphene-coated, few-layer water on mica.

Fourier transform infrared (FTIR) spectra on samples transferred in a final bath of H_2O and D_2O (99.9% purity) in Figure 1b. We subtract a reference mica signal from both the D_2O and H_2O transmission spectra, and then we renormalize the spectra to get absorbance information. The H_2O signal is noisy, as there is no H_2O IR-active peak in this range. However, the D_2O signal peaks around 2340 and 2360 cm^{-1}, corresponding to the symmetric and asymmetric stretch modes of the O−D bond.[40] There is a negligible amount of D_2O adsorbed on the graphene from ambient exposure, and thus we conclude that the graphene must be trapping the D_2O, as seen in CNTs.[40]

It is possible that the −OD group within D_2O could exchange with the interlayer −OH groups in muscovite mica. Still, we believe that this exchange is minimal in our graphene transfer, as previous work showed that this exchange within muscovite required many hours of 600 °C exposure to pressurized D_2O vapor.[41] These conditions are quite different than our transfer conditions. The sensitivity of IR measurements to D_2O monolayers under graphene is also worth noting. Sum-frequency generation (SFG) IR spectroscopy measurements of submonolayer, adsorbed D_2O on mica gave a O−D stretch mode at ~2375 cm^{-1}, demonstrating the sensitivity of their IR measurements to small amounts of D_2O (i.e., submonolayer to few-layer).[42] However, we note that this measurement, due to its configuration, was more sensitive than the conventional FTIR measurement that we performed, thereby making it possible that we have not encapsulated D_2O. Still, the higher amount of D_2O present in the wet transfer process likely implies that the signal in Figure 1b that we are observing is attributable to graphene-coated D_2O on

mica. Additional experimental[43] and theoretical[44] work of D_2O adsorbed on graphene show similar qualitative trends (e.g., a doubly peaked IR spectrum around 2500 cm^{-1}) to our observed FTIR spectra, albeit at higher wavenumbers. We attribute this shift due to graphene-induced D_2O confinement.[45]

Within Figure 1c, we show point Raman spectra (λ_{exc} = 633 nm) of graphene on mica. We transferred graphene in water and using a modified dry transfer[46] process (see the Supporting Information). For the graphene-coated water on mica, we show Raman spectra before and after a UHV high temperature degas at ~650 °C. We also give Raman spectra of the bare mica for reference. All graphene spectra are monolayer, as determined by the peak height I_{2D}/I_G ratio,[47] the 2D band position, and the 2D band full width at half-maximum (fwhm).[48] The dry transferred graphene possesses a G band at ~1595 cm^{-1}. Comparing the 2D band of the dry and wet (before degas) Raman spectra, one notes a red-shift of the 2D band to ~2647 cm^{-1} (wet transferred graphene at ~2652 cm^{-1}). Strain, either uniaxial, biaxial or inhomogeneous, can cause a peak position shift in the G and 2D bands and increase the G-band fwhm.[49,50] Thus, our Raman measurements on the wet, degassed, and dry transferred graphene films could reveal a combination of doping and strain. From the dry transferred graphene 2D band position and its fwhm (~44.8 cm^{-1}), we determine a tensile strain $\varepsilon \sim 0.25\%$, downshifting both the 2D and G bands. Applying this shift to the G band (averaging the contributions from the G$^-$ and G$^+$ bands) gives a ~1597 cm^{-1}, consistent with graphene on bare mica.[6] Still, graphene on bare mica[3] has a G-band fwhm of ~8 cm^{-1}, a factor of 2 lower than this band's fwhm of 16.3 cm^{-1}. The anomalously high fwhm originates

from the tensile strain as well as some inhomogeneous broadening[50] caused by wrinkles in the dry transfer process. Hence, the dry transferred graphene shows the effects of missing interfacial water on graphene on mica.

In the case of wet transfer, the PMMA/graphene stacks underwent a modified RCA clean[51] (SC-2 followed by SC-1) to eliminate adsorbed metal and organic contaminants that might dope the graphene from underneath. Both spectra are of monolayer graphene,[6,47] though the onset of the D and D′ bands indicates that the degassing process induced some defects (see the Supporting Information). Notably, the G band downshifts after the degas (from 1597 cm^{-1} to 1586 cm^{-1}), showing a change in doping.[52,53] Furthermore, its fwhm increases, implying that electron–phonon coupling is lessened by decreased doping.[53] The 2D band, however, shifts from 2651 cm^{-1} to 2666 cm^{-1} after the degas, the opposite direction of what is expected for the elimination of a p-type dopant.[53] Our analysis shows that the compressive strain required to satisfy the 2D band upshift post degas would subsequently upshift the G band, the opposite of what we observe. We give further discussion in the Supporting Information.

We hold that our 2D band upshift is due to local graphene band structure modification by strongly adsorbed PMMA at defects, similar to a previous report of annealed PMMA on graphene.[54] These effects are not seen in our STM measurements but are observed in the Raman measurements, as each method has different fundamental length scales. As discussed in the Supporting Information, the quasi-parabolic band structure of the PMMA/graphene decreases the Fermi velocity, thereby blue-shifting the 2D band strongly and barely modifying the G band.[55] Furthermore, the invariance of the peak height I_{2D}/I_G ratio before and after the degas suggests that we have not introduced additional dopants in our processing.[53] Thus, the post-degas Raman point spectrum is characteristic of CVD graphene on water on mica. Still, we provide spatial mapping to strengthen this conclusion further.

Figure 1d gives a histogram of the G-band position before the degas, a Gaussian distribution centered at 1596 cm^{-1} (population mean of $\langle\omega\rangle$ = 1595.0 ± 8.9 cm^{-1}, n = 89). A previous report[6] showed that the G band for graphene on bare mica is around ω_G ~ 1595 cm^{-1}. Despite the similarity in G-band position, we hold that many layers of water are encapsulated by the graphene during water-based transfer, as shown in Figure 1b. The introduction of this water, combined with its stability on mica,[56] makes it unlikely that we have graphene on bare mica during our Raman measurement. Before the degas in UHV, we find that STM imaging of the surface is unstable, which we attribute to adsorbed contaminants. Therefore, the high value of the G-band position likely originates from remaining p-type PMMA residue[57] from the graphene transfer. It is also possible that the many layers of water possess more residual dopants, shifting the G band. Doping effects are also present in other Raman metrics (see the Supporting Information).

After the ~650 °C degas, the G band's position shifts to 1586 cm^{-1} (population mean of $\langle\omega\rangle$ = 1585.9 ± 4.4 cm^{-1}, n = 129), as shown in the histogram of Figure 1e. The band's position is close to previous Raman measurements[6] for graphene on single-layer water on mica (ω_G ~ 1583 cm^{-1}). On the basis of earlier reports for annealed CVD graphene (in UHV[57] and in air[54]), it appears that the high temperature degas removed most of the adsorbed PMMA residue from the graphene, downshifting the G band. The $\Delta\omega_G$ ~ 3 cm^{-1} upshift between our

mean G-band position and the previously published work could be a sampling effect or could be attributed to p-type atmospheric adsorbates[53] and some remaining PMMA[51] within the Raman spot. Only a few points within the Raman map composing Figure 1e (see Supporting Information for the map) are near what is expected for graphene on bare mica, ~ 1595 cm^{-1}, supporting the conclusion that the graphene is covering a full, multilayered water film. The G band's lower position is due to the water screening interfacial charge transfer[6] between the graphene and heavily p-type mica. If graphene were p-type doped by the bare mica, we would expect a strong shift in the graphene Fermi level in scanning tunneling spectroscopy (STS) measurements. We do not see this, which we discuss in the Supporting Information.

Scrutinizing the G band fwhm carefully raises the concern of inhomogeneous broadening[50] in the Raman spot. The large spatial sampling over which the data in Figures 1c and 1d are collected makes it unlikely that the downshift in the G band and its broadened fwhm result from inhomogeneous broadening. However, if the thermal degas introduces wrinkles into the graphene, on a scale larger than the STM images but smaller than the Raman spot, inhomogeneous broadening could occur, thereby increasing the G-band fwhm. Thermally induced wrinkles in graphene and their effects on Raman were previously studied,[58] making this outcome feasible. However, we believe that doping is the dominant effect for the trends observed, but we cannot rule out inhomogeneous broadening entirely.

In Figure 2, we show a 30 nm by 30 nm STM topographic image of a typical sample surface (Figure 2a) and a zoomed-in spatial derivative (Figure 2b) illustrating the honeycomb lattice of the monolayer graphene covering. We present a larger 100 nm by 100 nm false-colored STM topograph in Figure 2c, which gives a better overview of our surface and shows the relative heights of the different features. There are three distinct water layers visible, as well as a graphene grain boundary and some taller protrusions extending from the top water layer. The presence of the grain boundary is not surprising, as CVD graphene is known to be polycrystalline,[59,60] but it is interesting to note that the water does not appear to preferentially congregate along the boundary. In light of recent AFM data suggesting that adsorbed water prefers to form droplets instead of layers centered on defects on hydrophobic surfaces,[29] we can conclude that the hydrophobicity of the CVD graphene covering has little effect on the underlying water structure.

It is possible that our high temperature degas in UHV induces strain in the graphene as the water escapes, which could deform the graphene[61,62] and influence the water structure that we observe. However, a recent AFM study demonstrated that water easily escapes from the edges of the graphene–mica interface,[14] which would imply that most of the volatile water would have already escaped during the pump down (0% relative humidity) process before degas. Also, the presence of intact low-angle grain boundaries[63] suggests that the remaining water does not exert enough pressure when heated to seriously damage the graphene. We do not notice any major changes in the surface structure for degas times ranging from 5 to 30 h. Temperature-induced stress deformities are generally large-scale wrinkles and should not affect the small surface features that we observe, such as the protrusions out of the top water layer.[62] The protrusions range from several angstroms to over 1 nm tall, and they only appear on the second or third water layer. This implies that their formation is dependent on the
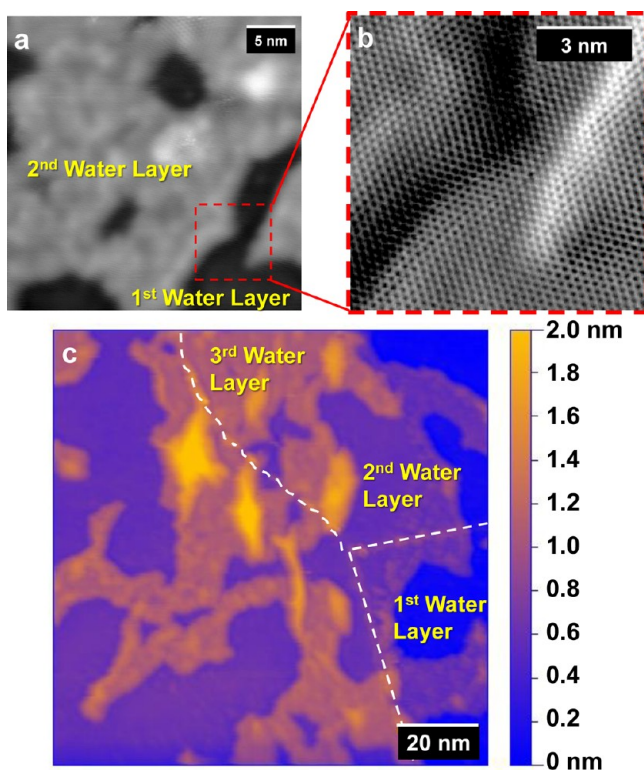
Figure 2. Scanning tunneling microscopy topographic scans of few-layered water confined between graphene and mica. (a) 30 nm by 30 nm image showing the first two water layers on the mica surface. (b) Zoomed-in spatial derivative of the boxed region in (a) showing the honeycomb lattice of the monolayer graphene coating. (c) 100 nm by 100 nm false-colored topographic image of graphene–water–mica system. Three layers of water are visible, as well as a graphene grain boundary, which is labeled by the dotted white line. The protrusions coming out of the third water layer could be due to either contaminants trapped under the graphene or to the water displaying increasing bulklike properties as it gets further from the mica surface. Scanning conditions are −0.35 V sample bias and 1 nA tunneling current.

underlying water structure rather than on the graphene coating. A more likely explanation for these protrusions would be that they are water-surrounded contaminants or perhaps nano-droplets that have nucleated out of defects in the mica. They could also be additional layers of water which have started to exhibit bulklike behavior due to their increasing distance from the mica surface. Molecular dynamics simulations and X-ray reflectivity data have indicated that water layers on mica cease to be easily distinguishable starting at around 1 nm away from the mica surface.[56,64] The water structures are also extremely stable over the course of our experimental observation (several days for some areas), regardless of the water layer or protrusion size.

We measure the exact number of trapped water layers by sandwiching single-walled carbon nanotubes (SWCNTs) between the graphene and mica. The SWCNTs are deposited onto the mica via ex-situ dry contact transfer[65] (DCT) before the graphene covering is applied. The mica is heated during DCT to ensure that any water is removed and the SWCNTs come into direct contact with the mica surface. We use HiPco SWCNTs with a narrow diameter distribution centered on 1 nm,[66] which means that we can use the measured height of these nanotubes to extract the number of water layers. A STM

topograph of a water-immersed SWCNT sandwiched between graphene and mica is shown in Figure 3a. Only part of the
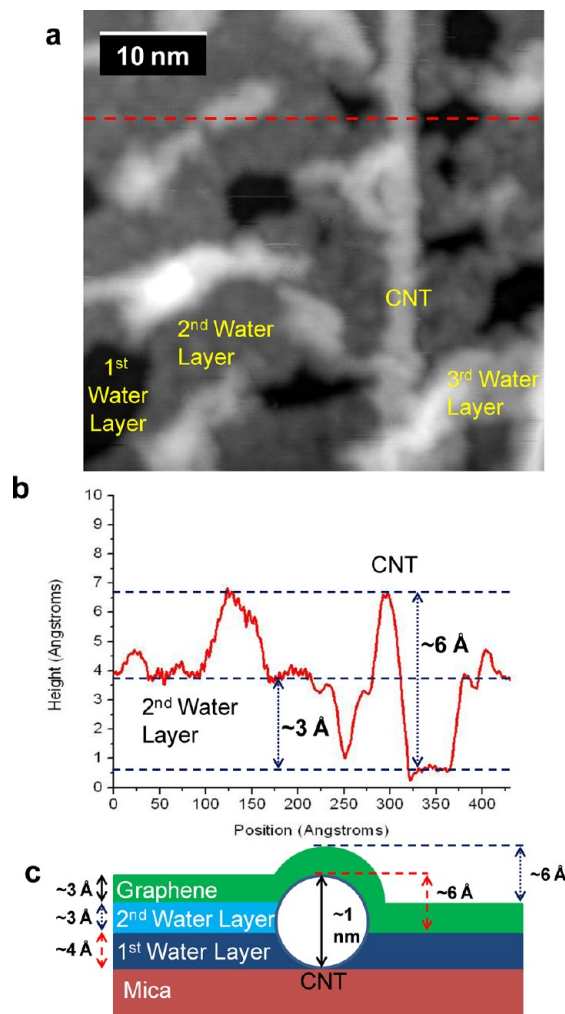
Figure 3. (a) 43 nm by 43 nm topographic STM image of a single-walled carbon nanotube embedded in the confined water layers between the graphene and mica. The first and second water layers are clearly defined, while the sporadic clusters appear to be the beginnings of a third water layer. (b) Height profile taken at the dotted red line in (a). Here, the second water layer appears to be ~3 Å tall, while the SWCNT juts 6 Å above the first water layer. (c) Cartoon showing how we determine the heights of each of the water layers in this image. The dotted blue arrows are the values that we measured in (b): 3 Å for the second water layer and 6 Å for the part of the SWCNT above the first water layer. The black arrows are the heights that we know from external references: ~3 Å in height for monolayer graphene and ~1 nm for our HiPco SWCNTs. The red arrows represent the heights that we derived from our known quantities. Knowing the total height (~1 nm) of our SWCNT and how much it juts out of the first water layer (~0.6 Å), we can subtract and determine that there is indeed only one layer of water between the graphene and mica and that the height of this layer is ~4 Å. Scanning conditions were −0.35 V sample bias and 1 nA tunneling current.

SWCNT is shown in the 43 nm by 43 nm scan; the total length of the nanotube is ~100 nm. There is a monolayer of water trapped between the SWCNT and the graphene coating, and this layer is removed using the STM tip before the height measurements are taken. More details on this process can be found in the Supporting Information. Figure 3b shows a height
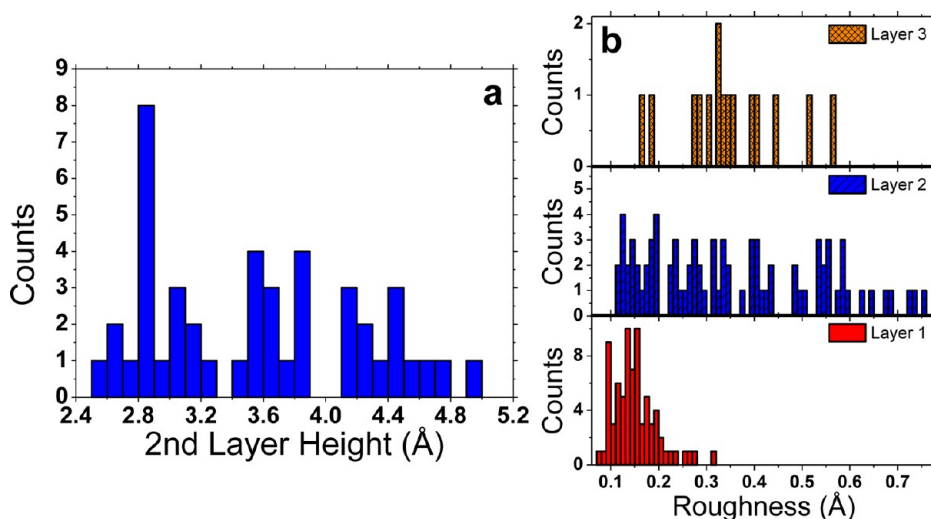
Figure 4. (a) Histogram of the height distribution of the second water layer. The data for this histogram were collected from four different samples, though each sample was prepared in a similar fashion. The average height is 3.5 Å, though the spread is quite large, and there is no clear trend. (b) Histogram of the roughness distribution for the three water layers that we have observed. These data were collected from the same four samples as the height measurements. We see that the roughness distribution of the first water layer is fairly narrow and centered at ∼15 pm, similar to AFM measurements reported previously. The roughness distribution for the second and third water layers, however, similar to the height distribution of the second water layer, is very spread out without a clear trend. This suggests that while the first layer may have a more well-defined structure, the second and third layers are amorphous.

profile taken at the dashed red line marked in Figure 3a. The height of the second water layer is measured to be ∼3 Å, and the difference in height between the SWCNT and the first water layer is ∼6 Å. Because of convolution with the tip geometry, the measured width of the SWCNT appears much broader than it actually is, but the height is unaffected by tip convolution and is a good gauge of the actual nanotube dimensions. Figure 3c shows a cartoon illustrating the different layer dimensions. The dotted blue arrows represent measured dimensions (second water layer height, difference in CNT height), the solid black arrows represent known dimensions (graphene height, total CNT height), and the dashed red arrows represent the calculated dimensions (first water layer height). Taking the difference between the measured height of the SWCNT (∼6 Å) and the known height of the SWCNT (∼10 Å), we can calculate the height of the water layer, which is ∼4 Å. This means that there is only 4 Å of water between the bottom layer shown in Figure 4a and the mica surface. This corresponds to approximately one layer of water and matches well with previous AFM data.[6,13]

In Figure 4, we present some statistics on the height and roughness of the water layers that we have sampled. These histograms include data from different regions on the same sample as well as data from several different samples. Figure 4a shows the height distribution of the second water layer. The heights are spread over a wide range (average of 3.5 Å), suggesting that this layer does not have a definite crystal structure. This observation is further corroborated in Figure 4b, which shows the roughness distribution of the water layers. The roughness of the second water layer has a wide range, suggestive of an amorphous structure. In contrast, the roughness of the first water layer is narrowly distributed and centered around 15 pm, similar to previous AFM measurements.[13]

To further explore the nature of the water trapped under the graphene monolayer, we attempt to manipulate the surface by standard STM nanolithography techniques.[67−69] Prior work

demonstrated that water films on mica could be perturbed using an AFM tip[70] at room temperature, though such manipulation has not been demonstrated with a graphene coating. STM manipulation of water films at room temperature had not been possible until now, but manipulation of water at cryogenic temperatures had been previously reported.[71−74]

Figure 5 shows the creation of local pinholes in the amorphous second and third water layers. Like the non-modified water, the induced pinholes are also extremely stable over time. The topographs and associated height contours show that the created pinholes penetrate all the way through to the water layer below while leaving the graphene undamaged. The size of these pinholes can be partially controlled by adjusting the electron dose and bias potential, though their shapes tend to be nonuniform and somewhat random. We are able to manipulate the water layer at both positive (Figure 5a,c) and negative (Figure 5b,d) sample bias, whereas existing work only reported successful manipulation at positive sample bias.[71−74] Of course, all previous STM manipulation work has been performed on metal substrates, where it is hypothesized that the metal surface states mediate the excitation of the water,[72,75] so it is likely that our mechanism for manipulation is quite different.

The locality of the patterns, even through bilayer graphene (see Supporting Information), implies that the tunneling electrons are bypassing the graphene coating and directly interacting with the water hydrogen bonds. The nonuniformity and randomness of the patterns also suggest that the electrons are traveling a small distance through the water after injection. The fact that we observe water manipulation at both positive and negative sample bias rules out an electric field effect, since the water always moves away from the tip, independent of field direction. Attempts to move the tip closer to the surface under zero bias showed us that manipulation did not occur as a result of the tip pushing into the water layer. Inelastic electron tunneling (IET) into the amorphous water layer does not explain the nonuniformity and the tendril-like spreading of the
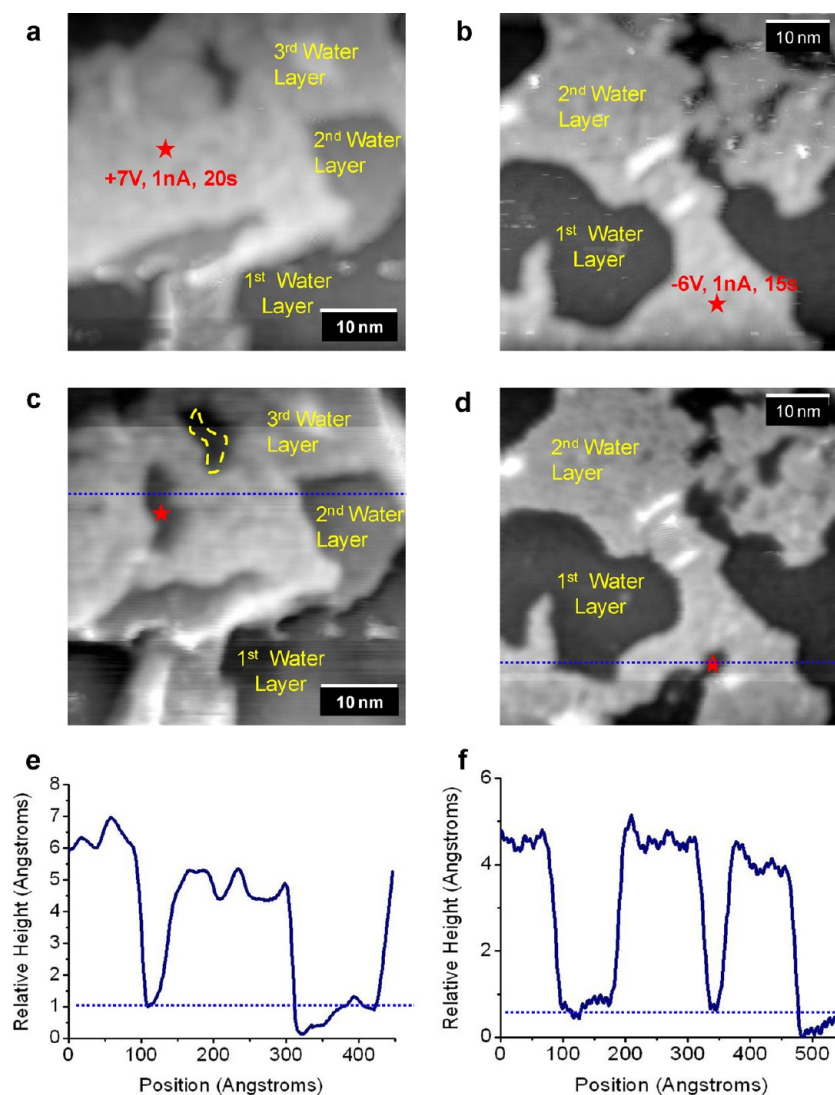
Figure 5. (a) STM topographic image of the third water layer before nanomanipulation at positive sample bias. (b) Topographic image of the second water layer before nanomanipulation at negative sample bias. (c) Topographic image of the same area in (a) after nanomanipulation at positive sample bias. The created pinhole is nonuniform, though it is localized to where the tip was centered. The dotted yellow line shows the outline of the original pinhole from (a), and we can see that this pinhole was also slightly enlarged after the manipulation. (d) Topographic image of the same area in (b) after nanomanipulation at negative sample bias. Similar to the positive bias case, the pinhole is again nonuniform and appears to propagate in a random direction. (e, f) Height contours showing that for both the positive and negative bias case the pinholes penetrate down to the water layer below. Scanning conditions were −0.35 V sample bias and 1 nA tunneling current.

patterns, as all of the patterning should be localized to right under the tip apex. It is possible that the tendril-like patterns are being created by Joule heating as the tunneling electrons dissipate through the water layer. The exact effect that the graphene has on these tunneling electrons as well as the states that these electrons are using is not obvious from our current data, and it will be the subject of a future systematic study.

Similar to previous AFM work,[13] we are unable to manipulate the first layer of water. This is most likely due to its crystalline structure and its strong adhesion to the hydrophilic mica surface. However, we do not believe the crystalline structure of the first water layer to be ice Ih, as previously claimed.[13] Ice Ih has a hexagonal lattice structure, which should form a hexagonal moiré pattern with the graphene lattice, depending on the relative alignment. We have imaged many different graphene orientations over the course of our experiments but have never observed a moiré pattern exclusive to the first water layer. The hexagonal moiré

patterns that we did observe were due to the presence of stacked graphene and were visible over all the water layers (see Supporting Information).

A possible explanation for the structure of the first water layer is that while it does not have a well-defined, periodic crystal structure, it is strongly bound to the mica surface. The hydration layer on mica has been the subject of many theoretical[64,76] and experimental studies,[8,10,56] though its exact thickness and behavior are still contested.[9,11] From our data, as well as previous research,[6,12,13,56,64] we argue that the thickness of the hydration layer on mica is ∼1 nm and is split into three distinct water layers. The first water layer is strongly bound to the mica surface, with a thickness of ∼4 Å. This layer cannot be manipulated and exhibits properties similar to a crystalline solid. The second and third water layers, on the other hand, while still more viscous than bulk water, are much more amenable to manipulation than the first layer. They are stable in equilibrium at room temperature, but high tunneling

conditions can break bonds and cause them to rearrange. Beyond layer three, the water begins to exhibit bulk-like behavior, as the layers start to blend together.

In summary, we performed Raman spectroscopy and UHV-STM at room temperature on few-layered water trapped between monolayer graphene and mica. The graphene coating keeps the water stable on the surface and protects it from high temperature processing in vacuum. It does not otherwise perturb or alter the water bonding structure, even at the higher defect-density grain boundaries. We observe up to three layers of water trapped between the graphene and mica, with the first layer being ordered and strongly bound. Consequently, the second and third layers are amorphous. We also demonstrate the ability to manipulate the amorphous water layers using the STM tip. This work shows the feasibility of using CVD graphene coatings for nanotemplating in high resolution STM studies and furthers our understanding of water behavior near the mica surface. Graphene-coated water will allow further STM-based research of other aqueous suspended structures, such as biomolecules in water.

■ ASSOCIATED CONTENT

Ⓢ Supporting Information

Experimental methods; optical microscopy images; additional Raman spectra and analysis; STM images of turbostratic bilayer graphene; scanning tunneling spectroscopy (STS) data for graphene on water on mica; the procedure used for height and roughness analysis of our water layers; and graphene grain boundary imaging by STM. This material is available free of charge via the Internet at http://pubs.acs.org.

■ AUTHOR INFORMATION

Corresponding Author
*E-mail: lyding@illinois.edu.

Author Contributions
[⊥]These authors contributed equally.

Notes
The authors declare no competing financial interest.

■ ACKNOWLEDGMENTS

■ REFERENCES

(1) Verdaguer, A.; Sacha, G. M.; Bluhm, H.; Salmeron, M. *Chem. Rev.* **2006**, *106*, 1478–510.
(2) Thiel, P. A.; Madey, T. E. *Surf. Sci. Rep.* **1987**, *7*, 211–385.
(3) Brown, G. E. *Science* **2001**, *294*, 67–69.
(4) Guckenberger, R.; Heim, M.; Cevc, G.; Knapp, H. F.; Wiegräbe, W.; Hillebrand, A. *Science* **1994**, *266*, 1538–1540.
(5) Jang, C.; Adam, S.; Chen, J.-H.; Williams, E. D.; Das Sarma, S.; Fuhrer, M. S. *Phys. Rev. Lett.* **2008**, *101*, 146805.
(6) Shim, J.; Lui, C. H.; Ko, T. Y.; Yu, Y.-J.; Kim, P.; Heinz, T.; Ryu, S. *Nano Lett.* **2012**, *12*, 648–654.
(7) Israelachvili, J. N.; Pashley, R. M. *Nature* **1982**, *300*, 341.
(8) Israelachvili, J. N.; Pashley, R. M. *Nature* **1983**, *306*, 249.
(9) Israelachvili, J. N.; Wennerström, H. *Nature* **1996**, *379*, 219.
(10) Raviv, U.; Klein, J. *Science* **2002**, *297*, 1540–1543.
(11) Granick, S.; Bae, S.; Kumar, S.; Yu, C. *Physics* **2010**, *3*, 1.
(12) Khan, S.; Matei, G.; Patil, S.; Hoffmann, P. *Phys. Rev. Lett.* **2010**, *105*, 106101–1–106101–4.
(13) Xu, K.; Cao, P.; Heath, J. R. *Science* **2010**, *329*, 1188–91.
(14) Severin, N.; Lange, P.; Sokolov, I. M.; Rabe, J. P. *Nano Lett.* **2012**, *12*, 774.
(15) Geim, A. K.; Novoselov, K. S. *Nat. Mater.* **2007**, *6*, 183–191.
(16) Geim, A. K. *Science* **2009**, *324*, 1530–4.
(17) Zhang, Y.; Tan, Y.-W.; Stormer, H. L.; Kim, P. *Nature* **2005**, *438*, 201–4.
(18) Bolotin, K. I.; Sikes, K. J.; Jiang, Z.; Klima, M.; Fudenberg, G.; Hone, J.; Kim, P.; Stormer, H. L. *Solid State Commun.* **2008**, *146*, 351–355.
(19) Novoselov, K. S.; Geim, A. K.; Morozov, S. V.; Jiang, D.; Zhang, Y.; Dubonos, S. V.; Grigorieva, I. V.; Firsov, A. A. *Science* **2004**, *306*, 666–9.
(20) Novoselov, K. S.; Geim, A. K.; Morozov, S. V.; Jiang, D.; Katsnelson, M. I.; Grigorieva, I. V.; Dubonos, S. V.; Firsov, A. A. *Nature* **2005**, *438*, 197–200.
(21) Kim, R.; Bae, M.; Kim, D. G.; Cheng, H.; Kim, B. H.; Kim, D.; Li, M.; Wu, J.; Du, F.; Kim, H.; Kim, S.; Estrada, D.; Hong, S. W.; Huang, Y.; Pop, E.; Rogers, J. A. *Nano Lett.* **2011**, *11*, 3881.
(22) Rutter, G. M.; Guisinger, N. P.; Crain, J. N.; Jarvis, E. A. A.; Stiles, M. D.; Li, T.; First, P. N.; Stroscio, J. A. *Phys. Rev. B* **2007**, *76*, 235416.
(23) Schedin, F.; Geim, A. K.; Morozov, S. V.; Hill, E. W.; Blake, P.; Katsnelson, M. I.; Novoselov, K. S. *Nat. Mater.* **2007**, *6*, 652–5.
(24) Ishigami, M.; Chen, J. H.; Cullen, W. G.; Fuhrer, M. S.; Williams, E. D. *Nano Lett.* **2007**, *7*, 1643–8.
(25) Ritter, K. A.; Lyding, J. W. *Nat. Mater.* **2009**, *8*, 235–242.
(26) He, K. T.; Koepke, J. C.; Barraza-Lopez, S.; Lyding, J. W. *Nano Lett.* **2010**, *10*, 3446–52.
(27) Cao, P.; Xu, K.; Varghese, J. O.; Heath, J. R. *J. Am. Chem. Soc.* **2011**, *133*, 2334–7.
(28) Mohanty, N.; Fahrenholtz, M.; Nagaraja, A.; Boyle, D.; Berry, V. *Nano Lett.* **2011**, *11*, 1270–5.
(29) Cao, P.; Xu, K.; Varghese, J. O.; Heath, J. R. *Nano Lett.* **2011**, *11*, 5581–6.
(30) Bunch, J. S.; Verbridge, S. S.; Alden, J. S.; van der Zande, A. M.; Parpia, J. M.; Craighead, H. G.; McEuen, P. L. *Nano Lett.* **2008**, *8*, 2458–2462.
(31) Lui, C. H.; Liu, L.; Mak, K. F.; Flynn, G. W.; Heinz, T. F. *Nature* **2009**, *462*, 339–41.
(32) Lee, C.; Li, Q.; Kalb, W.; Liu, X.-Z.; Berger, H.; Carpick, R. W.; Hone, J. *Science* **2010**, *328*, 76–80.
(33) Wood, J. D.; Schmucker, S. W.; Lyons, A. S.; Pop, E.; Lyding, J. W. *Nano Lett.* **2011**, *11*, 4547–4554.
(34) Li, X.; Cai, W.; An, J.; Kim, S.; Nah, J.; Yang, D.; Piner, R.; Velamakanni, A.; Jung, I.; Tutuc, E.; Banerjee, S. K.; Colombo, L.; Ruoff, R. S. *Science* **2009**, *324*, 1312–4.
(35) Zhang, W.; Wu, P.; Li, Z.; Yang, J. *J. Phys. Chem. C* **2011**, *115*, 17782–17787.
(36) Bhaviripudi, S.; Jia, X.; Dresselhaus, M. S.; Kong, J. *Nano Lett.* **2010**, *10*, 4128–33.
(37) Li, X.; Zhu, Y.; Cai, W.; Borysiak, M.; Han, B.; Chen, D.; Piner, R. D.; Colombo, L.; Ruoff, R. S. *Nano Lett.* **2009**, *9*, 4359–63.
(38) Wu, Z.; Chen, Z.; Du, X.; Logan, J. M.; Sippel, J.; Nikolou, M.; Kamaras, K.; Reynolds, J. R.; Tanner, D. B.; Hebard, A. F.; Rinzler, A. G. *Science* **2004**, *305*, 1273–6.
(39) Nair, R. R.; Blake, P.; Grigorenko, A. N.; Novoselov, K. S.; Booth, T. J.; Stauber, T.; Peres, N. M. R.; Geim, A. K. *Science* **2008**, *320*, 1308.
(40) Ellison, M. D.; Good, A. P.; Kinnaman, C. S.; Padgett, N. E. *J. Phys. Chem. B* **2005**, *109*, 10640–6.
(41) Vedder, W.; McDonald, R. S. *J. Chem. Phys.* **1963**, *38*, 1583.
(42) Miranda, P.; Xu, L.; Shen, Y.; Salmeron, M. *Phys. Rev. Lett.* **1998**, *81*, 5876–5879.

(43) Kimmel, G. A.; Matthiesen, J.; Baer, M.; Mundy, C. J.; Petrik, N. G.; Smith, R. S.; Dohnálek, Z.; Kay, B. D. *J. Am. Chem. Soc.* **2009**, *131*, 12838−44.

(44) Donadio, D.; Cicero, G.; Schwegler, E.; Sharma, M.; Galli, G. *J. Phys. Chem. B* **2009**, *113*, 4170−5.

(45) Crupi, V.; Interdonato, S.; Longo, F.; Majolino, D.; Migliardo, P.; Venuti, V. *J. Raman Spectrosc.* **2008**, *39*, 244−249.

(46) Suk, J. W.; Kitt, A.; Magnuson, C. W.; Hao, Y.; Ahmed, S.; An, J.; Swan, A. K.; Goldberg, B. B.; Ruoff, R. S. *ACS Nano* **2011**, *5*, 6916−24.

(47) Ferrari, A. *Solid State Commun.* **2007**, *143*, 47−57.

(48) Lenski, D. R.; Fuhrer, M. S. *J. Appl. Phys.* **2011**, *110*, 013720.

(49) Huang, M.; Yan, H.; Chen, C.; Song, D.; Heinz, T. F.; Hone, J. *Proc. Natl. Acad. Sci. U. S. A.* **2009**, *106*, 7304−8.

(50) Berciaud, S.; Ryu, S.; Brus, L. E.; Heinz, T. F. *Nano Lett.* **2009**, *9*, 346−52.

(51) Liang, X.; Sperling, B. A.; Calizo, I.; Cheng, G.; Hacker, C. A.; Zhang, Q.; Obeng, Y.; Yan, K.; Peng, H.; Li, Q.; Zhu, X.; Yuan, H.; Hight Walker, A. R.; Liu, Z.; Peng, L.-M.; Richter, C. A. *ACS Nano* **2011**, *5*, 9144−9153.

(52) Malard, L. M.; Pimenta, M. A.; Dresselhaus, G.; Dresselhaus, M. S. *Phys. Rep.* **2009**, *473*, 51−87.

(53) Das, A.; Pisana, S.; Chakraborty, B.; Piscanec, S.; Saha, S. K.; Waghmare, U. V.; Novoselov, K. S.; Krishnamurthy, H. R.; Geim, A. K.; Ferrari, A. C.; Sood, A. K. *Nat. Nanotechnol.* **2008**, *3*, 210−5.

(54) Lin, Y.-C.; Lu, C.-C.; Yeh, C.-H.; Jin, C.; Suenaga, K.; Chiu, P.-W. *Nano Lett.* **2012**, *12*, 414−419.

(55) Ni, Z.; Wang, Y.; Yu, T.; You, Y.; Shen, Z. *Phys. Rev. B* **2008**, *77*, 113407.

(56) Cheng, L.; Fenter, P.; Nagy, K.; Schlegel, M.; Sturchio, N. *Phys. Rev. Lett.* **2001**, *87*, 156103.

(57) Pirkle, A.; Chan, J.; Venugopal, A.; Hinojos, D.; Magnuson, C. W.; McDonnell, S.; Colombo, L.; Vogel, E. M.; Ruoff, R. S.; Wallace, R. M. *Appl. Phys. Lett.* **2011**, *99*, 122108.

(58) Chen, C.-C.; Bao, W.; Theiss, J.; Dames, C.; Lau, C. N.; Cronin, S. B. *Nano Lett.* **2009**, *9*, 4172−6.

(59) Huang, P. Y.; Ruiz-Vargas, C. S.; van der Zande, A. M.; Whitney, W. S.; Levendorf, M. P.; Kevek, J. W.; Garg, S.; Alden, J. S.; Hustedt, C. J.; Zhu, Y.; Park, J.; McEuen, P. L.; Muller, D. A. *Nature* **2011**, *469*, 389−92.

(60) Koepke, J. C.; Wood, J. D.; Estrada, D.; Ong, Z. Y.; Pop, E.; Lyding, J. W. Submitted for review, 2012.

(61) Levy, N.; Burke, S. A.; Meaker, K. L.; Panlasigui, M.; Zettl, A.; Guinea, F.; Castro Neto, A. H.; Crommie, M. F. *Science* **2010**, *329*, 544−7.

(62) Sutter, P.; Sadowski, J. T.; Sutter, E. *Phys. Rev. B* **2009**, *80*, 245411.

(63) Grantab, R.; Shenoy, V. B.; Ruoff, R. S. *Science* **2010**, *330*, 946−8.

(64) Park, S.-H.; Sposito, G. *Phys. Rev. Lett.* **2002**, *89*, 085501.

(65) Albrecht, P. M.; Lyding, J. W. *Appl. Phys. Lett.* **2003**, *83*, 5029.

(66) HiPco Carbon Single Walled Carbon Nanotubes, http://www.nanointegris.com/en/hipco (accessed Feb 15, 2012).

(67) Lyding, J. W.; Hubacek, J. S.; Tucker, J. R.; Abeln, G. C.; Shen, T.-C. *Appl. Phys. Lett.* **1994**, *64*, 2010.

(68) Shen, T. C.; Wang, C.; Abeln, G. C.; Tucker, J. R.; Lyding, J. W.; Avouris, P.; Walkup, R. E. *Science* **1995**, *268*, 1590−2.

(69) Xu, Y.; He, K. T.; Schmucker, S. W.; Guo, Z.; Koepke, J. C.; Wood, J. D.; Lyding, J. W.; Aluru, N. R. *Nano Lett.* **2011**, *11*, 2735−42.

(70) Xu, L.; Lio, A.; Hu, J.; Ogletree, D. F.; Salmeron, M. *J. Phys. Chem. B* **1998**, *102*, 540−548.

(71) Morgenstern, K.; Rieder, K.-H. *Chem. Phys. Lett.* **2002**, *358*, 250−256.

(72) Gawronski, H.; Carrasco, J.; Michaelides, A.; Morgenstern, K. *Phys. Rev. Lett.* **2008**, *101*, 196101.

(73) Mehlhorn, M.; Gawronski, H.; Morgenstern, K. *Phys. Rev. Lett.* **2008**, *101*, 196101.

(74) Morgenstern, K.; Rieder, K.-H. *J. Chem. Phys.* **2002**, *116*, 5746.

(75) Maksymovych, P.; Dougherty, D.; Zhu, X.-Y.; Yates, J. *Phys. Rev. Lett.* **2007**, 99.

(76) Odelius, M.; Bernasconi, M.; Parrinello, M. *Phys. Rev. Lett.* **1997**, *78*, 2855−2858.

Supplemental Information

Scanning Tunneling Microscopy Study and Nanomanipulation of Graphene-Coated Water on Mica

Kevin T. He[1,3†], Joshua D. Wood[1,2,3†],Gregory P. Doidge[1,2,3], Eric Pop[1,2,3], Joseph W. Lyding[1,3*]

[1]Department of Electrical and Computer Engineering,
[2]Micro and Nanotechnology Lab,
[3]Beckman Institute for Advanced Science and Technology,
University of Illinois at Urbana-Champaign, Urbana, IL 61801, USA.

[†]These authors contributed equally

[*]Corresponding author. E-mail: lyding@illinois.edu

Contents:

I. Methods

For samples not employing carbon nanotubes (CNT) as a height reference, we used 1.4 mil copper foil (Basic Copper, Carbondale, IL USA) in a hot-wall Atomate CVD system. These Cu foils were pre-annealed at ~1000 °C under Ar/H_2 flow for 45 min, and we grew graphene at ~1000 °C with 100 sccm of CH_4, 50 sccm of H_2, and 1000 sccm of Ar for 30 min following a previously published procedure.[1] The operating pressure during growth was ~0.5 torr. The resulting substrates were cooled to room temperature at ~20 °C/min under the same gas flow. We cleaned mica (SPI Inc., V-1 grade muscovite) and a razor blade with acetone, isopropanol, and DI water rinses. Using the razor blade, we cleaved the freshly cleaned mica. We coated the graphene/Cu surface with a 495K A2 and 950K A4 PMMA bilayer (MicroChem). Each PMMA layer was spin coated at 3000 RPM for 30 s and cured at 200 °C for 2 min. The graphene on Cu backside was removed by an O_2 plasma in a reactive ion etcher (RIE). An additional protective layer of 950K A4 PMMA was spun on and cured using the same parameters to protect the graphene film. The Cu foil was then etched by 1M $FeCl_3$ etchant overnight. Using a cleaned glass slide, the remaining graphene film was transferred to a DI water bath for ~5 min followed by a second DI bath to further clean the graphene from etchant residues. We transferred the film to the cleaned mica surface in the second DI bath. The PMMA was stripped with a 1:1 methylene chloride to methanol bath for 20 min, followed by annealing at 400 °C in Ar/H_2 for 1 hr.

For samples employing CNTs as a height reference, we deposited HiPco CNTs (Unidym, Inc. lot #R0223) by *ex-situ* dry contact transfer (DCT)[2,3] at elevated temperature (> 100 °C) to prevent water adsorption on the mica. The mica (SPI Inc.) was cleaved three times with scotch tape rather than a razor blade, giving a flatter overall mica surface with larger crystal planes. We confirmed the presence of CNTs by atomic force microscopy (AFM). For graphene growth, we used 1 mil copper foil (Alfa Aesar, 99.8% purity) in the same hot-wall Atomate CVD system. The pre-anneal and growth flow rates were the same as the previous samples, except for a decrease in CH_4 flow rate to 75 sccm to increase the percentage of monolayer graphene. Similarly, we coated the graphene/Cu surface with the same PMMA bilayer (MicroChem). Each PMMA layer was spin coated at 3000 RPM for 30 s and cured at 200 °C for 2 min. The graphene on Cu backside was removed by an O_2 plasma in a RIE. The Cu foil was then etched by commercial Cu etchant, CE-100 ($FeCl_3$ base, Transene Co.) overnight. Using a cleaned glass slide, the remaining graphene film was transferred to a DI water bath for ~15 min. The PMMA/graphene film was cleaned in a room-temperature, modified RCA clean. In this clean, SC-2 (20:1:1 $H_2O:H_2O_2:HCl$, concentrated) was followed by SC-1 (20:1:1 $H_2O:H_2O_2:NH_4OH$, concentrated) for 15 min each to eliminate metal and organic contaminants underneath the graphene. We transferred the film to another DI bath, in which we transferred the film to the mica surface with CNTs on it. The PMMA was stripped with an acetone bath for 20 min, followed by annealing at 400 °C in Ar/H_2 for 1.5 hr.

Dry transferred samples were made by growing graphene on 1 mil Cu (Alfa Aesar, 99.8% purity) using 75 sccm of CH_4 and 50 sccm of H_2 at 1000 °C for 25 min. The operating pressure during growth was ~0.5 torr. The resulting substrates were cooled to room temperature at

~20 °C/min under the same gas flow. PMMA was coated on the graphene on Cu and the backside and Cu were etched following the above procedure. The PMMA film was cleaned with 3 DI water baths, ~15 min each. A piece of cured PDMS was cleaned using methanol, acetone, and IPA, and it was dried with N_2. This PMMA-fluid meniscus was inverted onto the PDMS so that the PMMA was flipped onto the PDMS. Thus, the stack had the following order from the top: graphene, PMMA, and PDMS. The exposed graphene top side was carefully dried with N_2 and placed in a Fluoroware container. It was then placed on top of hot (~150 °C), freshly cleaved mica (on a hot plate), and a heavy weight forced the PDMS/PMMA/graphene stack into contact with the mica. The system was kept at that temperature for ~18 hrs to make the PMMA glassy and bring about good graphene adhesion. The PDMS stamp was then removed rapidly, leaving some PMMA residue on the dry transferred graphene on mica.

A 270 nm gold contact was sputtered onto the samples using a shadow mask. We used a homebuilt, room-temperature UHV system with a base pressure of ~5×10^{-11} torr for scanning tunneling microscopy measurements. The sample was degassed in the UHV-STM system by direct-current heating through a n+ Si backing at a temperature of ~650-700 °C for several hours. We acquired STS data using standard lock-in techniques. Our STM tips are made of etched tungsten wire and sharpened using field directed sputtering.[4]

Raman spectroscopy was taken using a Renishaw Raman microsope (inVia and WiRE 3.2 software) with 20x and 50x objectives, 1800 lines/mm grating, 30 s acquisition time, ~1.8-9 mW power, and 633 nm laser excitation, unless otherwise noted. Raman maps were analyzed by fitting single Lorentzians around the 2D (also called G'), G, and D bands, centered at 2690 cm^{-1}, 1580 cm^{-1}, and 1350 cm^{-1}, respectively. A six point polynomial background was subtracted before Lorentzian fitting. G peak position data were considered physical if their values were greater than 1570 cm^{-1} and less than 1630 cm^{-1}. 2D band full width at half maxima (FWHM) were considered physical if their values were greater than 0 cm^{-1} and less than 60 cm^{-1}. Fourier transform infrared (FTIR) spectroscopy was performed with a Thermo Scientific Nicolet 6700 FTIR. Data was spaced with 2 wavenumber resolution, and 64 scans were taken for both the background mica and the graphene-water-mica samples.

II. Optical Microscopy

We determined the amount of CVD graphene coverage on our transparent mica substrates using optical microscopy, shown in figure S1. For figure S1(a), we transferred PMMA-coated graphene into a final DI H_2O bath. Figure S1(a) shows tears and folds in the film, which can give some the turbostratic bilayer regions seen by STM. Moreover, the film has noticeable PMMA residue from the transfer. In figure S1(b), we transferred PMMA-coated graphene into a final D_2O (99.9% pure) water bath. Films were in both baths for ~1 min before transfer onto the final mica substrate. The film of figure S1(b) looks similar to the DI water transferred film in figure S1(a).
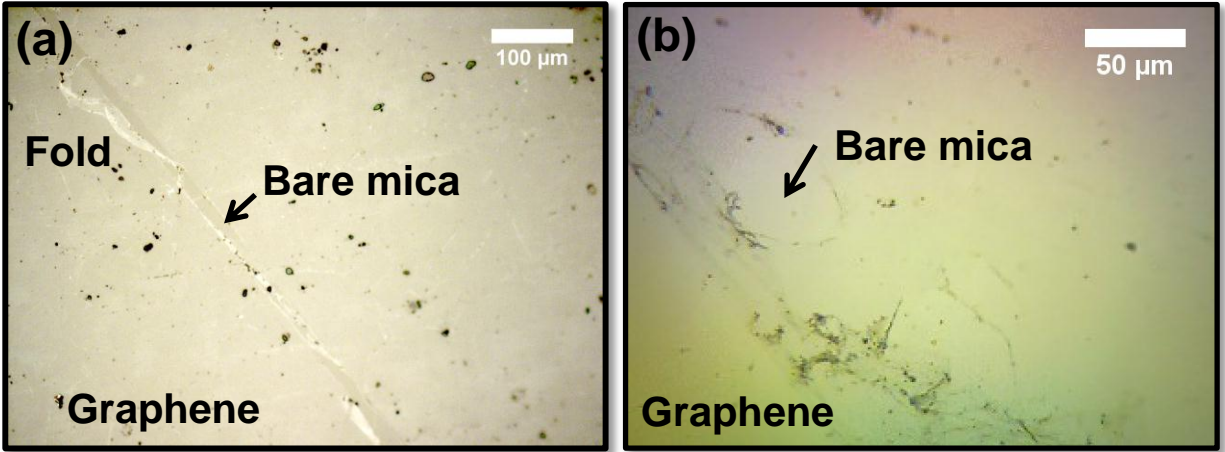
Figure S1. (a) Optical microscope image of DI water transferred graphene on mica. Folds, tears, and PMMA residue apparent in the image. **(b)** Optical microscope image of D_2O transferred graphene on mica. Similar tears and PMMA residue are present.

III. Raman Spectroscopy

To assess both graphene and trapped water coverage, we used Raman spectroscopy. In figures S2(a) and S2(b), we give spatial Raman spectra maps for transferred CVD graphene on mica. These maps are overlaid on the optical image in which they were taken. We then took a ratio of the Lorentzian peak intensity under the 2D (G') and G Lorentzian curves for figure S2(a) and the Lorentzian G band position for S2(b). Most of the points in figure S2(a) are above 2 (peak height), indicative of monolayer graphene[5] or turbostratically stacked graphene. The G band positions within figure S2(b) are greater than 1590 cm^{-1} (see Fig. 1d), showing that there is doping on the graphene film from residual PMMA. We note that there is probably remaining PMMA after the acetone liftoff, as these samples did not undergo an Ar/H_2 anneal to remove PMMA. Within figure S2(c), we show a spatial map of I_D/I_G (peak not area ratio), giving graphene defect density and sp^3 character. Raman spectra taken on the Cu foil after growth did not show an appreciable D band, so we attribute its presence in the map to the graphene transfer. Furthermore, residual PMMA has been shown to contribute to the D band's intensity by increasing the amount of sp^3 carbon present.[6]
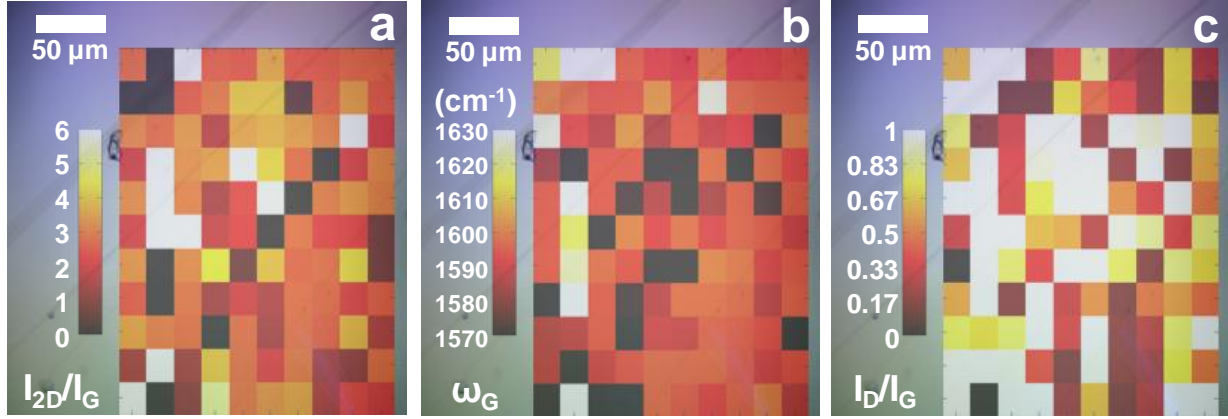
Figure S2. Spatial Raman mapping at λ_{exc} = 633 nm and 20X objective for RCA cleaned graphene transferred to mica in water. **(a)** Monolayer peak height I_{2D}/I_G map, showing evidence of monolayer or turbostratic graphene. **(b)** G band position map of the same area in (a), giving a high value for the G band position due to adsorbed PMMA and residual dopants. The histogram in Fig. 1d is derived from this figure. **(c)** Defect density I_D/I_G (peak intensity from fitted Lorentzians) map of the same area in (a). There are minor defects induced by the transfer as well as contributions from residual PMMA.

To determine whether the graphene is not turbostratically stacked from growth, one must look at the 2D band's FWHM. For Raman taken with λ_{exc} = 633 nm, it is known that turbostratically stacked CVD graphene increases the 2D FWHM from its expected value of ~30-35 cm^{-1} to ~45-55 cm^{-1}.[7] Further, turbostratically stacked graphite has been shown to blue-shift the 2D band[8] from its known position at ~2655 cm^{-1} for λ_{exc} = 633 nm to ~2663 cm^{-1}. Within figure S3(a), we see that the 2D FWHM is γ_{2D} = 31.4 ± 9.5 cm^{-1} (n = 100), close to the value expected for monolayer and not turbostratic graphene. In figure S3(b), the 2D peak position is ω_{2D} = 2650.6 ± 7.2 cm^{-1} (n = 74), red-shifted from its known position. Within the error, there is not an appreciable up-shift expected for a turbostratic sample. This discussion, combined with the fact that the peak height (from Lorentzian fits) I_{2D}/I_G is greater than 2 for most of the sample within figure S2 (and figure 1d in the main manuscript), makes us conclude that our samples are predominantly monolayer graphene.
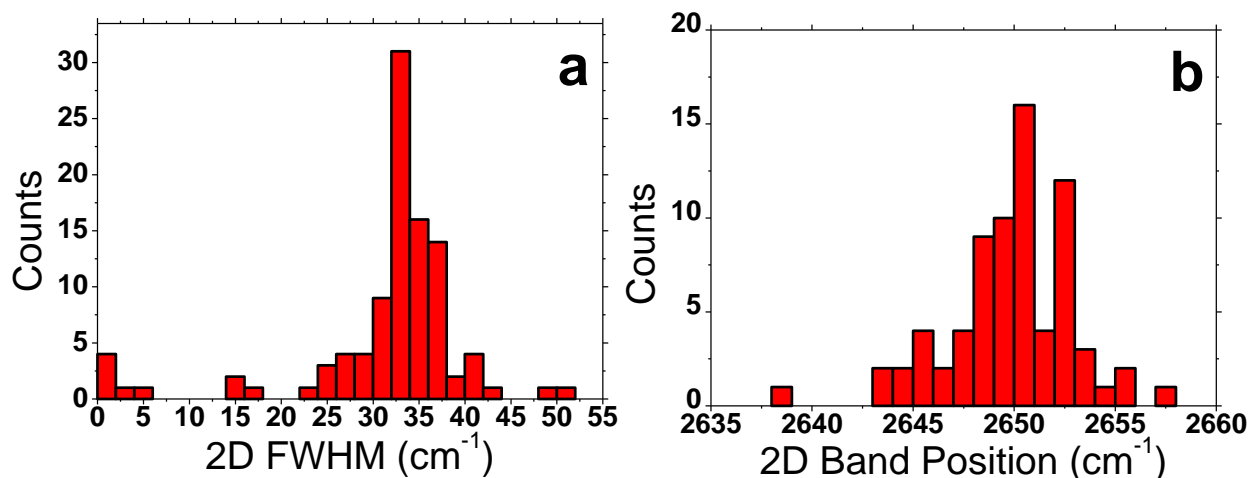
Figure S3. Evidence of monolayer CVD graphene on mica. **(a)** Histogram of the 2D band's full width at half maximum (FWHM) for the region mapped in figure S2. Distribution is centered around ~32 cm^{-1}, consistent with monolayer CVD graphene. **(b)** Histogram of the 2D band's position (Lorentzian fitted), centered at ~2650 cm^{-1}. This is also representative of monolayer graphene.

In figure S4, we show Raman spatial maps for the mica sample after the ~650 °C degas. Figure S4(a) shows that the peak height I_{2D}/I_G has decreased considerably. If the graphene were etched – thereby leading to a missing 2D and G band – then the film's conductivity would decrease, making STM scanning more difficult after the degas. We do not have any difficulty in bringing our STM tips into range with the surface after the degas, emphasizing the fact that the graphene on mica surface is still conducting. The decrease within the peak height I_{2D}/I_G is presumably due to higher disorder within the film and a possible increase in doping.[9] This higher disorder is made more evident in figure S4(c), showing the I_D/I_G (peak, not area) ratio for the same area as S4(a). Despite this increase in disorder, the G band's position – as shown in figure S4(b) – is uniform, with values centered about ~1585 cm^{-1}. This is not near the value expected for graphene on bare mica (~1595 cm^{-1}) and closer to the value for graphene on water on mica (~1583 cm^{-1}), showing that there is still water under the graphene. Moreover, this indicates that most of the PMMA on the surface has been removed in the UHV degas, but not at without introducing more disorder. The difficulty in removing PMMA without introducing disorder was previously shown.[10]

During the 650 °C degas, the mica should expand and the graphene should contract, possibly becoming a source of uniaxial, biaxial, or inhomogeneous strain.[11,12] This strain can consequently cause the positions of the 2D and G band to shift. Moreover, the strain softens the G phonons, increasing the G band FWHM; this could lead to the doping shifts (G band downshift) and the increase in G band FWHM that we observe in our Raman data after the degas. Figure S5 gives a schematic diagram of the shifts that would occur for the simultaneous removal of doping and addition of strain for the 2D and G bands. Within figure S5(a), we

estimate the sample's doping shift due to the evaporation of PMMA, using recent reports for annealed CVD graphene.[13] Starting from $<\omega_{2D}> = 2651$ cm^{-1} ($n = 99$), this loss of PMMA ($\Delta p \sim 10^{12}$ cm^{-2}) should downshift the 2D band by 3 cm^{-1}, giving $\omega_{2D,PMMA} = 2648$ cm^{-1}. The final position of the band is at $<\omega_{2D,degas}> = 2666$ cm^{-1} ($n = 73$). To arrive at this final band position, one must uniaxially apply a compressive shift[11] to the graphene of $\varepsilon = 0.9 \pm 0.2\%$. We then use this compressive shift when analyzing the G band in figure S5(b), initially at $<\omega_G> = 1597$ cm^{-1} ($n = 71$). The compressive strain will upshift the G band after removing the contribution due to PMMA doping (a downshift). Strain will also split the G band into separate G$^-$ and G$^+$ (with respect to energy) bands, whose splitting is best observed by polarized Raman spectroscopy; the value of strain from S5(a) will give upshifts of 4.8 cm^{-1} and 2.1 cm^{-1}, respectively. Averaging these shifts gives an overall upshift of 3.5 cm^{-1} for the unsplit G band. This is the incorrect direction for the observed final G band position at $<\omega_G> = 1588$ cm^{-1} ($n = 20$). Thus, we must conclude that data cannot be explained by a compressive shift and decreased doping.

An alternative approach to explaining the data considers the effect of the degas on the residual PMMA. Lin *et al.*[10] showed that PMMA which is adsorbed at defects (i.e., wrinkles and grain boundaries) is difficult to remove with temperature processing. Their work also argued that temperature processed PMMA can modulate the linear band structure of graphene. All of their Raman data – both on SiO$_2$ and suspended – showed an anomalous blue-shift for the 2D band; they claimed that these blue-shifts were not attributable to strain and that they originated from an approximately parabolic PMMA/graphene dispersion under the Raman spot. For a parabolic dispersion ($E = \hbar^2 k^2/(2m^*)$) the Fermi velocity v_F scales as k ($v_F \sim k$), which at low energy gives velocities two orders of magnitude less than the Fermi velocity in pristine graphene ($v_{F =} 1$ x 10^6 m/s). The 2D band shift can be approximated at double-resonance as $\Delta\omega_{2D} \approx [E_L - \hbar\omega_{2D}D_{2D}/2]\Delta v_F/(\hbar v_F^2)$, where E_L is the laser energy (eV), and D_{2D} is the phonon dispersion at the K (K') point (eV·Å).[14] Though most of the PMMA is removed by the degas, it is likely that some PMMA still exists at grain boundaries and defects in our CVD films. Our STM images do not show strongly adsorbed PMMA on graphene, but the large size of the Raman spot relative to the area sampled by STM makes observing these larger-scale effects possible. This annealed PMMA/graphene, with its quasi-parabolic dispersion, should lower the Fermi velocity and blue-shift the 2D band relative to the pre-degas 2D band position. We also note that the blue-shift in the 2D band from this PMMA interaction ($\Delta\omega_{2D} = 18$ cm^{-1}) is close to previously observed value for annealed PMMA on suspended graphene ($\Delta\omega_{2D} = 13\pm6$ cm^{-1}).[10] It was formerly noted that the G band's position did not substantially change with a modification of the Fermi velocity.[14,15] Therefore, we can attribute the G band downshift and broadened FWHM in our data to decreased PMMA doping, and the 2D band upshift to band structure modification.
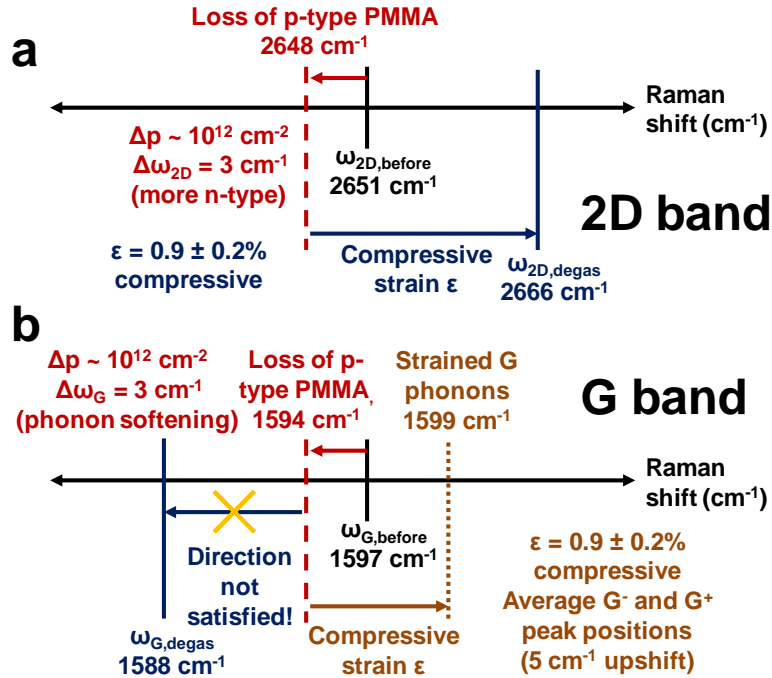
Figure S5. Elucidating the 2D and G band position shifts for the graphene on mica system before and after the degas. (a) 2D band position diagram, showing how the loss of PMMA (decreased doping) and onset of compressive strain from the degas gives the final band position. (b) G band position diagram, which also highlighting the combination of doping and strain within the CVD graphene. The final G band position observed – at ~1588 cm^{-1} – cannot be achieved by using doping and strain working in concert, as is the case in (a). Thus, the band's shift and increase in FWHM must be due to doping and another factor. We hold that it is doping and band structure modification.[10]

IV. Atomic Force Microscopy (AFM)

With a Bruker Dimension IV AFM, we performed tapping mode AFM using 300 kHz resonant frequency Si cantilevers on our wet transferred graphene on mica. We show a representative AFM image in figure S5. The image has considerable PMMA residue present, and there are wrinkles and tears in the graphene film. With these large features, we cannot use AFM to discern the finer water features that were visible in STM. Additionally, our tips had large radii of curvature (we estimate ~40 nm or more), making these fine water features hard to see, even in clean regions.
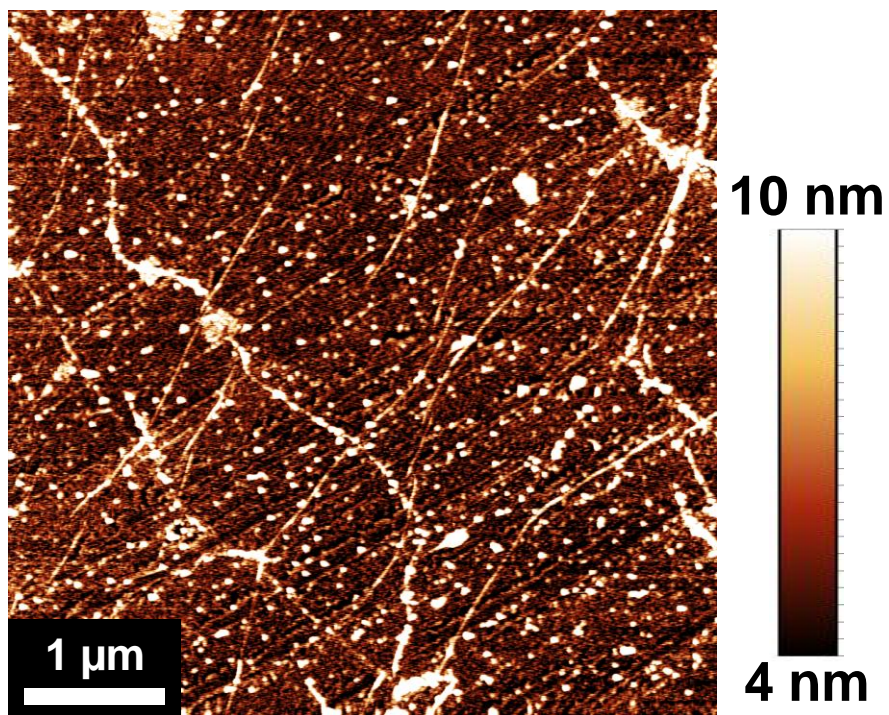
Figure S6. Atomic force microscopy (5 μm x 5 μm) image of graphene wet transferred to mica. The image shows wrinkles, holes, and PMMA residues from the transfer. The high roughness of these features makes observing fine water features difficult, even at smaller length scales (less than 5 μm).

V. Scanning Tunneling Spectroscopy (STS)

STS shows that there is very little difference in the location of the Dirac point when comparing graphene on one layer of water and graphene on two layers of water. It also shows that there is no p-doping of the graphene (indicated by the lack of a Dirac point offset from zero bias), which has been demonstrated to occur for graphene on bare mica.[16] This is consistent with previous Raman and scanning Kelvin probe microscopy measurements demonstrating that few-layered water screens graphene from the doping effects of the mica substrate.[16]
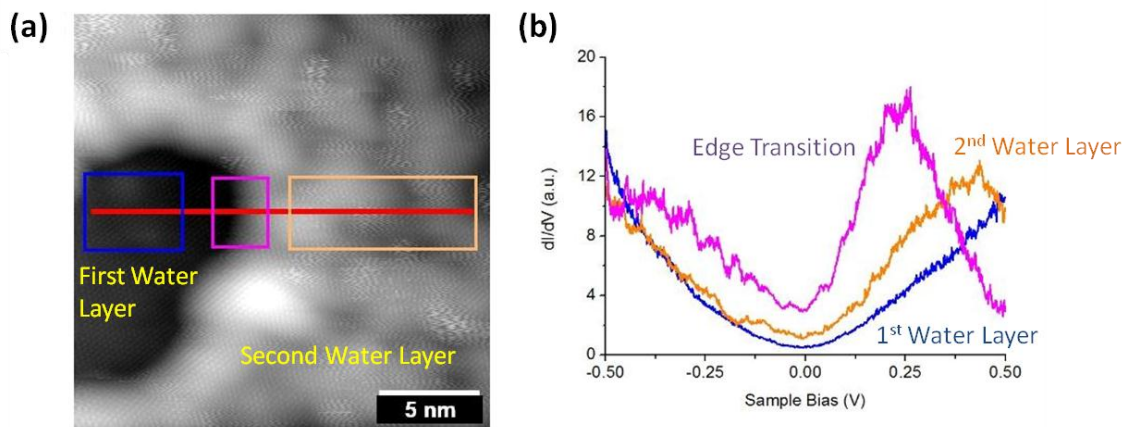
Figure S7. Scanning tunneling spectroscopy (STS) characterization of graphene on mica. **(a)** STM topograph with spectroscopy taken along the red line. **(b)** Averaged dI/dV data from the colored boxes in (a), showing a surface state at ~0.25 V at the edge of the transition between the first and second water layers. The Dirac points are all centered at zero bias, indicating the lack of graphene doping. The spectra were taken with standard lock-in techniques and 1 nA setpoint current. STM image taken at -0.35 V sample bias and 1 nA tunneling current.

VI. Graphene Grain Boundaries

CVD graphene on copper is usually made up of many graphene grains, with sizes that can range up to several microns each.[17,18] Here we show some more examples of these graphene grain boundaries. Figures (a) and (c) are grain boundaries on bilayer graphene (hence the hexagonal moiré pattern) while (b) and (d) are on monolayer graphene. Figure (d) is the same STM scan as Figure 2c in the manuscript, but without the false coloring and with the dashed white lines removed to better showcase the grain boundary. In all cases, we note that the underlying water does not preferentially adsorb to the graphene grain boundaries.
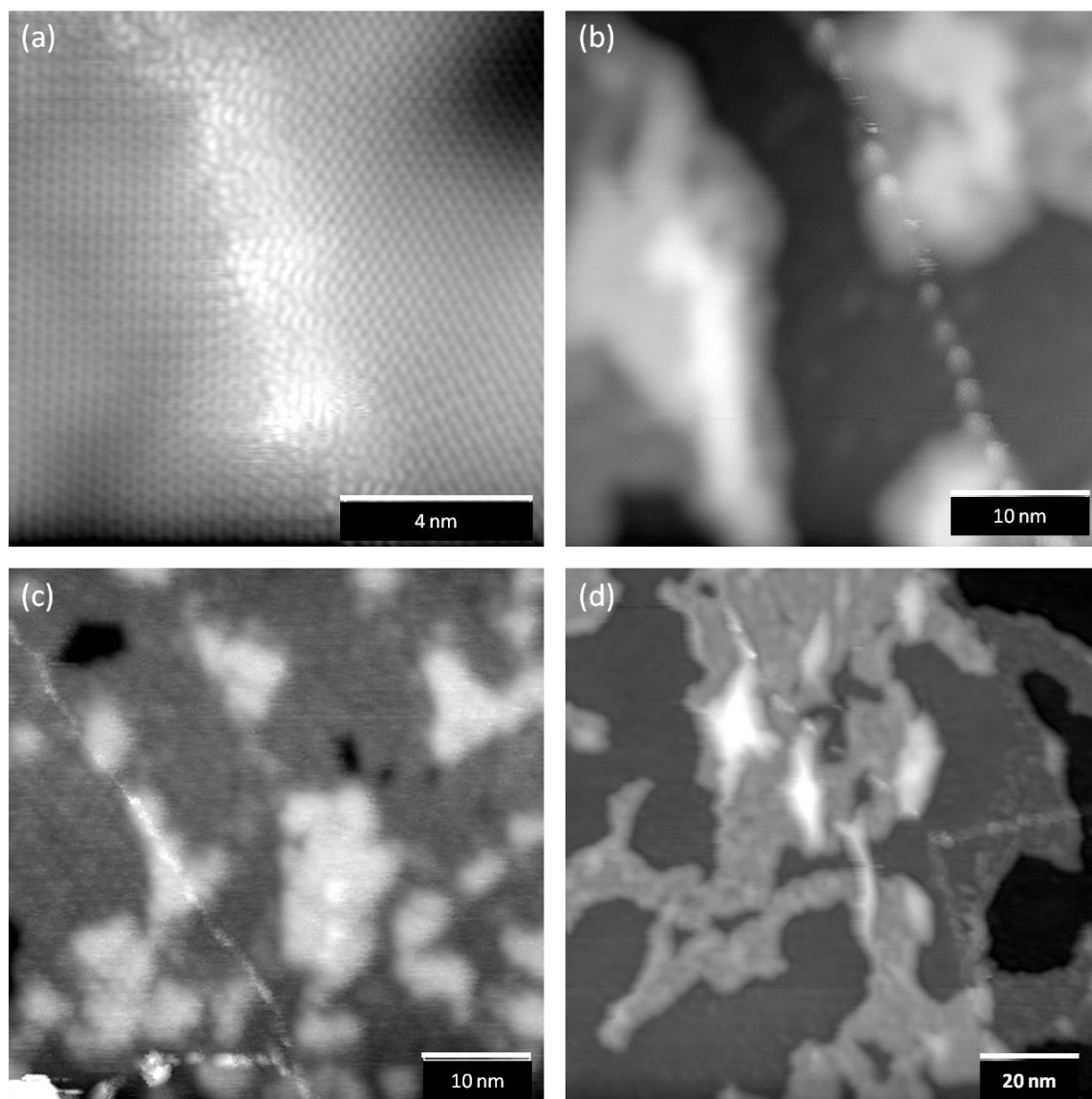
Figure S8. Examples of CVD graphene grain boundaries on water/mica. **(a)** A graphene grain boundary on bilayer graphene. **(b)** A graphene grain boundary on monolayer graphene. **(c)** An intersection of three graphene grain boundaries on bilayer graphene. **(d)** Another intersection of three graphene grains, this time on monolayer graphene. This is the same scan as Figure 2c in the manuscript, though the dotted white lines have been removed to make the grain boundaries easier to see. All scanning conditions are -0.35 V sample bias and 1 nA tunneling current.

VII. Effects of Degas Time

We do not notice any major changes in the graphene-water-mica system's structure for degas times in UHV ranging from 5 to 30 hours at 650 °C. The degas is performed by running current through a resistive silicon piece backing the graphene-water-mica sample. The sample temperature is determined using a pyrometer. The following STM topographic scans were taken on the same sample for the labeled degas times and temperatures. The surface structure is similar in both cases, though the tip is a little blunter in the 5-hour degas image.
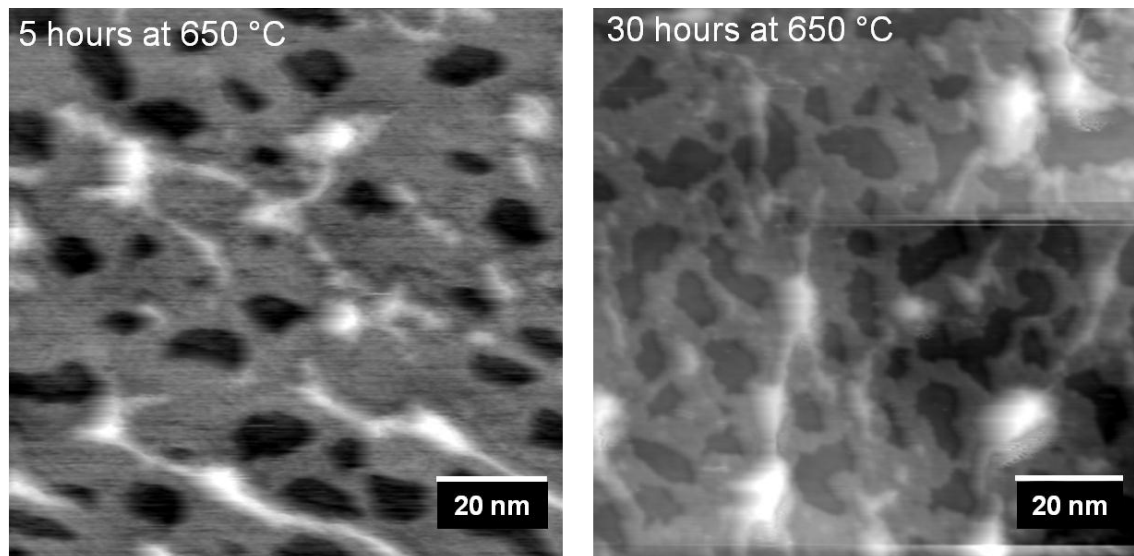
Figure S9. Comparison of the same sample surface after different degas times in UHV. There is no significant difference in the surface structure between these two scans. Scanning conditions were -0.35 V sample bias and 1 nA tunneling current.

VIII. Bilayer Graphene

Along with monolayer graphene, our transfer process also produces regions of bilayer graphene. It is possible to confuse the hexagonal moiré pattern formed on bilayer graphene that is not Bernal stacked with the hexagonal moiré pattern that one might expect to see for graphene on ice Ih. In our case, we know that we have bilayer graphene due to the observance of grain boundaries in the buried graphene layer.
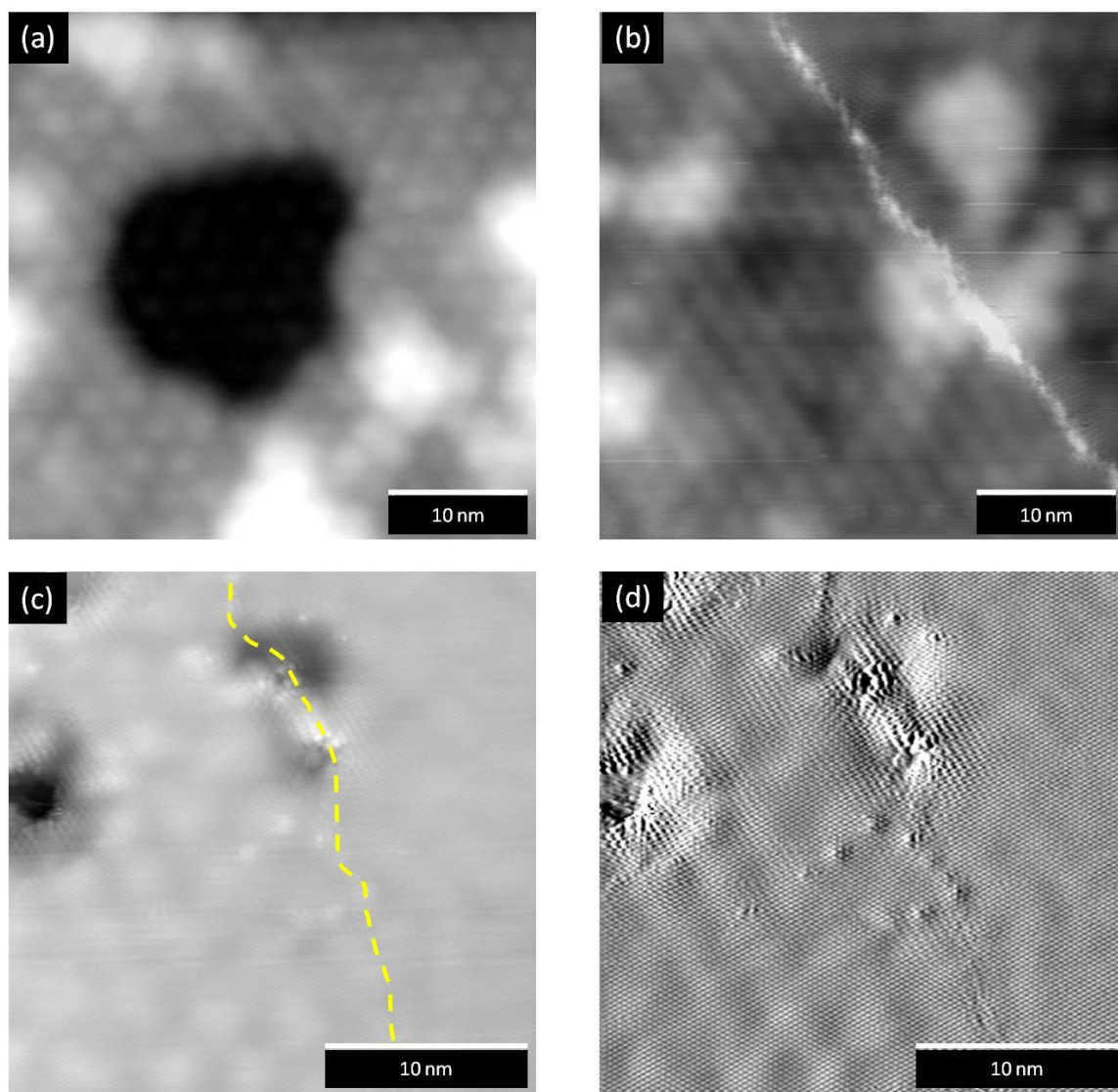
Figure 10. **(a)** STM topograph of a water trapped between bilayer graphene and mica. The moiré pattern is due to interference between the mismatched graphene lattices. **(b)** Another image of water trapped under bilayer graphene. The moiré pattern changes at the graphene grain boundary due to a rotation of the top graphene sheet. **(c)** Image of a buried graphene grain boundary, which is highlighted by the yellow dashed line. The top graphene layer is continuous, but there is a change in orientation of the underlying graphene layer due to the grain boundary. This is highlighted by the changes in moiré pattern at the grain boundary. **(d)** Spatial derivative of the image in (c) where the buried grain boundary is more obvious.

IX. Water Manipulation on Bilayer Graphene

This is a region of bilayer graphene where we are able to locally manipulate the water layer below. The manipulation conditions used are similar to those used on monolayer graphene. The locality of the created pinhole suggests that the tunneling current from the STM tip is

directly interacting with the water layer, since it is unlikely that it would travel through two layers of graphene without dispersing at least a little bit.
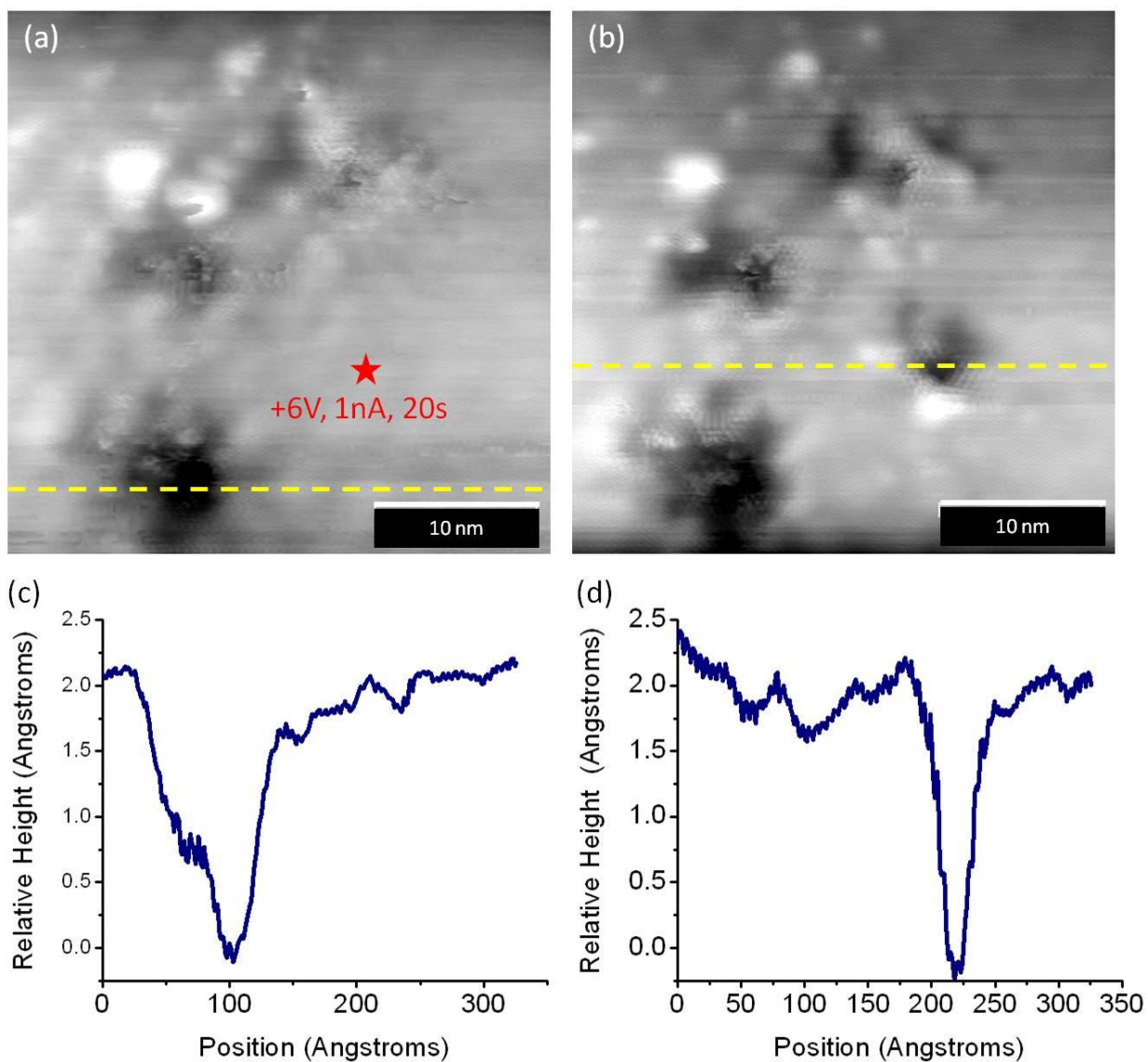
Figure S11. Localized patterning of water under bilayer graphene. **(a)** Before image, where we see three pre-existing holes, which were previously patterned. **(b)** Newly patterned hole seen at the location marked in (a). **(c)** Topographic line trace along the dashed line show in (a), indicating a hole depth of ~2 angstroms. **(d)** Topographic line trace of the newly patterned hole (dashed line in (b)).

X. Height and Roughness Measurements

We use the following method to measure the heights of roughness of our surface. We first plane fit our image to ensure that everything is leveled. This can be difficult for larger scans, so sometimes one large scan is broken up into several smaller pieces and each piece is plane fit and analyzed separately. We next take a height histogram of the image, as seen in (b) and (d). The major peaks in the histogram each represent one of the water layers. The peaks are fit using Gaussian distributions: the distance between the centers of these Gaussian fits is taken as the layer height while the standard deviation is taken as the layer roughness. We have much more measurements of layer roughness than layer height since roughness measurements can be taken on a flat region on the same layer, while for height you need two layers, ideally with both making a major contribution to the histogram. There is also an issue where larger scans have water layers with a larger apparent roughness than smaller scans, which is why these scans have a first water layer roughness that are outliers in our roughness distribution chart.
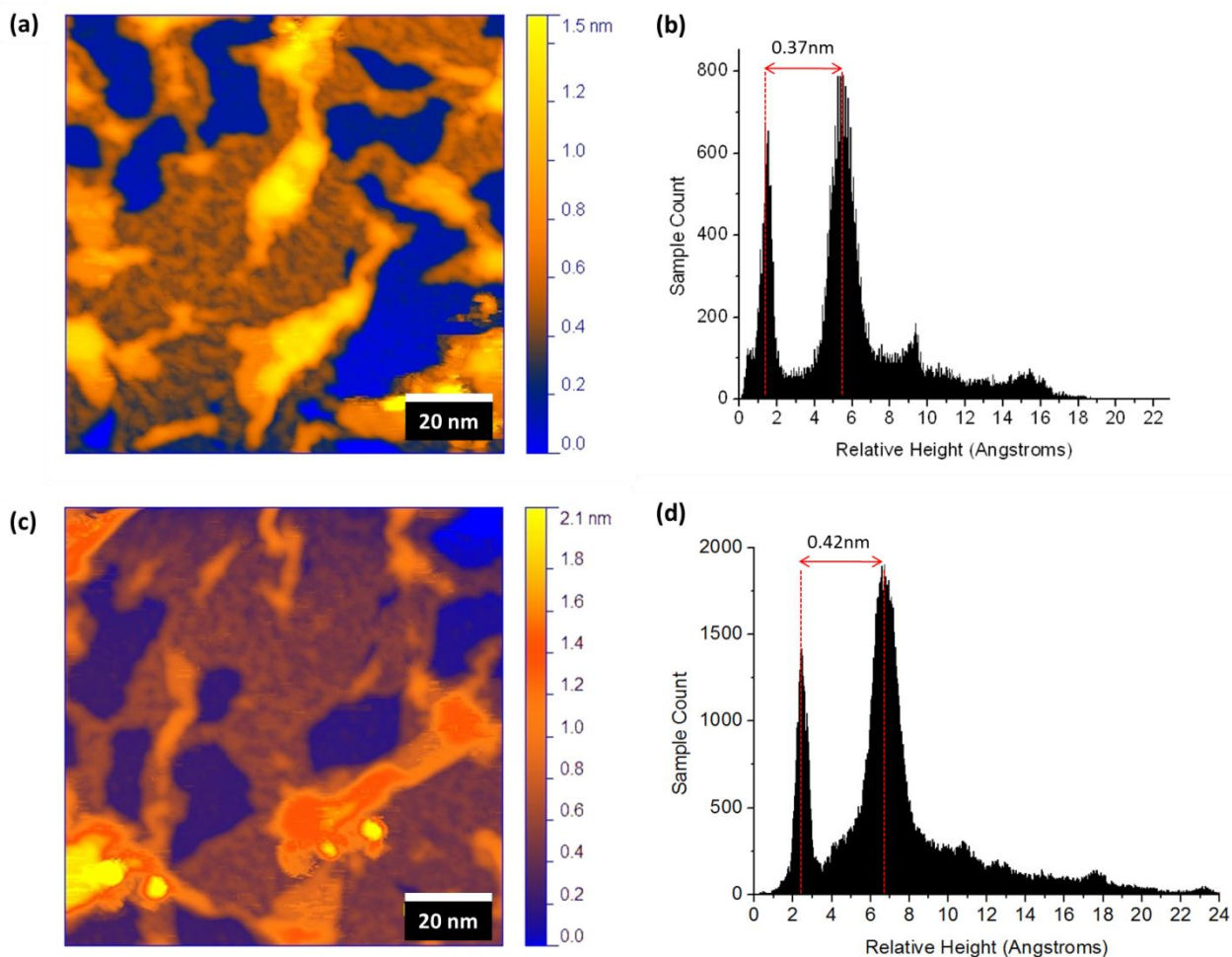

Figure S12. **(a)** False-colored topographic image and **(b)** associated height histogram. The height of the second water layer is this case is 3.7 Å and the standard deviations are 27 pm for the first layer and 61 pm for the second layer. **(c)** Another example of a false-colored topographic image and **(d)** height histogram. The height of the second water layer in this case is 4.2 Å and the standard deviations are 30 pm for the first layer and 82 pm for the second layer.

## XI. Differentiating CNTs from Water Structures

Along with SWCNTs, there are also many water structures that populate our surface, as shown in figure S13. In order to differentiate the CNTs from the water structures, we perturb them with the STM tip, using similar parameters as the water manipulation described in the main manuscript. The non-CNT water structures are easily damaged by the STM tip, but the CNTs maintain their shape. This can be seen in figure S14.

In figures S14(c) and S14(d), we notice that although the shape of the CNT does not change, there appears to be a reduction in the CNT height after manipulation. This change in height is more precisely shown in figure S15, where the manipulated region is ~2.5 Å shorter than the non-manipulated region. We believe that this height change is due to a monolayer layer of water trapped between the CNT and graphene coating being removed, as a water monolayer is approximately 2.5 Å tall. All of our CNT height measurements are performed with water layer removed.
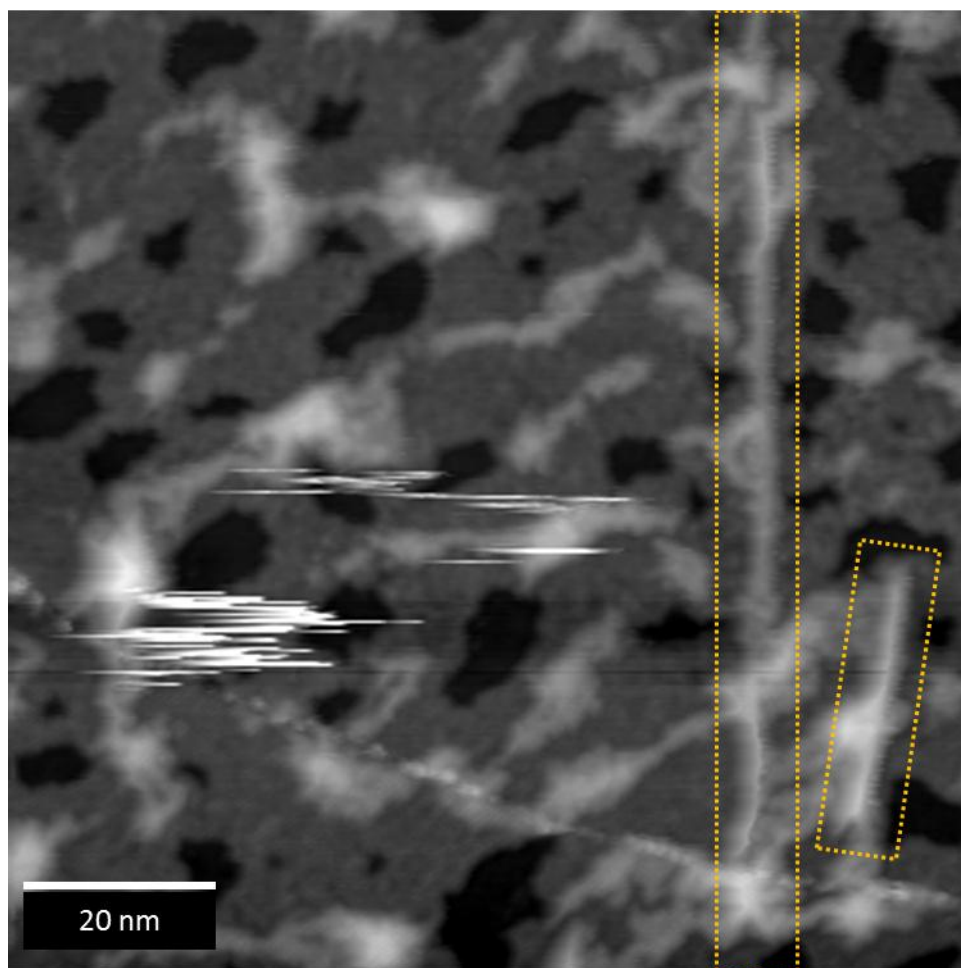

Figure S13. Large area STM topographic scan of two SWCNTs encased in few-layered water between a graphene coating and mica substrate. The SWCNTs are marked with the dotted orange boxes. All the other linear strand-like features are water structures. Scanning conditions are -0.35 V sample bias at 1 nA tunneling current.
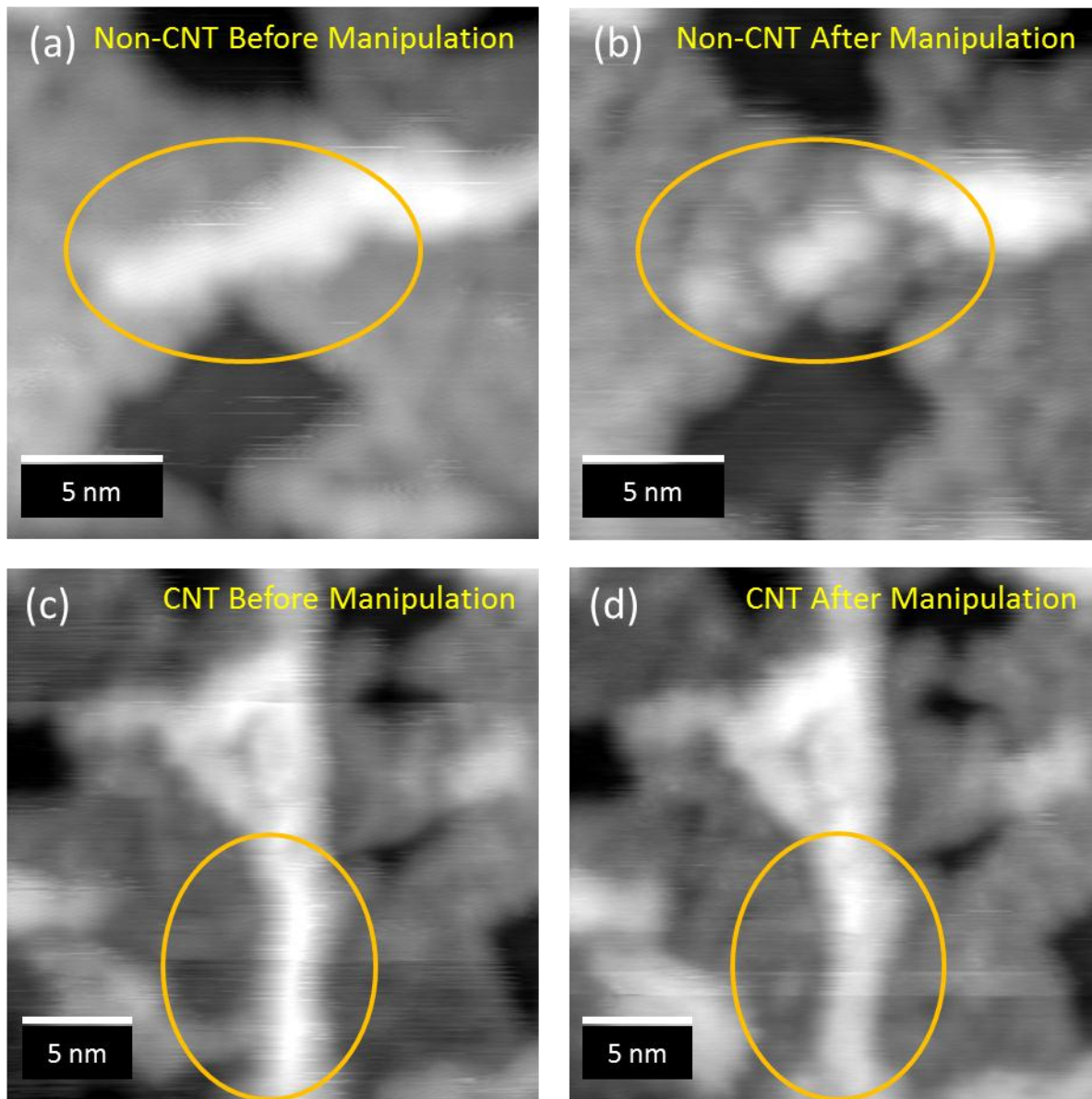
Figure S14. A STM topographic image of a linear water structure (a) before and (b) after manipulation using the STM tip. The water structure is clearly damaged and no longer holds its shape. A CNT (c) before and (d) after manipulation. The structure holds its shape, despite the surrounding water being moved. Scanning conditions are -0.35 V sample bias and 1 nA tunneling current.
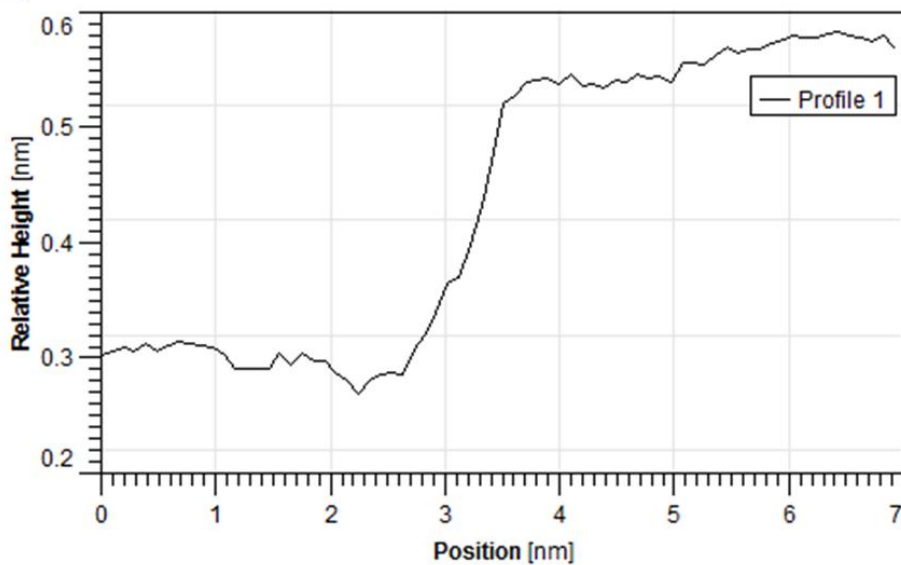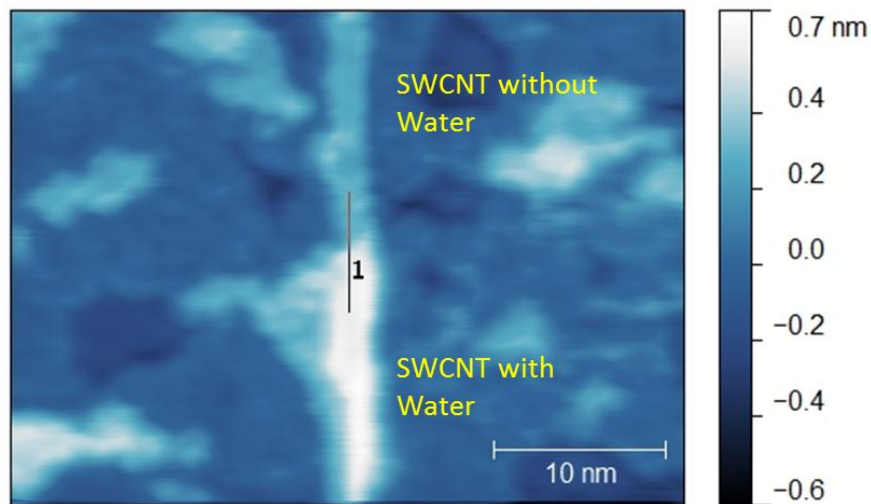
Figure S15. Sections of the same SWCNT with and without a layer of trapped water between itself and the graphene coating. The height contour is taken at the line labeled '1', and shows that the water layer trapped between the SWCNT and graphene is ~2.5 Å thick.

References

(1)   Wood, J. D.; Schmucker, S. W.; Lyons, A. S.; Pop, E.; Lyding, J. W. *Nano Letters* **2011**, *11*, 4547-4554.

(2)   Albrecht, P. M.; Lyding, J. W. *Applied Physics Letters* **2003**, *83*, 5029.

(3)   Ritter, K. A.; Lyding, J. W. *Nanotechnology* **2008**, *19*, 015704.

(4)   Schmucker, S. W.; Kumar, N.; Abelson, J. R.; Daly, S. R.; Girolami, G. S.; Lyding, J. W. *Nature Communications* **2012***, In Press*.

(5)   Ferrari, A. C.; Meyer, J. C.; Scardaci, V.; Casiraghi, C.; Lazzeri, M.; Mauri, F.; Piscanec, S.; Jiang, D.; Novoselov, K. S.; Roth, S.; Geim, A. K. *Physical Review Letters* **2006**, *97*.

(6)   Lin, Y.-M.; Valdes-Garcia, A.; Han, S.-J.; Farmer, D. B.; Meric, I.; Sun, Y.; Wu, Y.; Dimitrakopoulos, C.; Grill, A.; Avouris, P.; Jenkins, K. a *Science* **2011**, *332*, 1294-7.

(7)   Lenski, D. R.; Fuhrer, M. S. *Journal of Applied Physics* **2011**, *110*, 013720.

(8)   Jorio, A.; Dresselhaus, M.; Saito, R. *Raman spectroscopy in graphene related systems*; 2011; pp. 288-289.

(9)   Das, A.; Pisana, S.; Chakraborty, B.; Piscanec, S.; Saha, S. K.; Waghmare, U. V.; Novoselov, K. S.; Krishnamurthy, H. R.; Geim, A. K.; Ferrari, A. C.; Sood, A. K. *Nature Nanotechnology* **2008**, *3*, 210-5.

(10)   Lin, Y.-C.; Lu, C.-C.; Yeh, C.-H.; Jin, C.; Suenaga, K.; Chiu, P.-W. *Nano Letters* **2012**, *12*, 414-419.

(11)   Huang, M.; Yan, H.; Chen, C.; Song, D.; Heinz, T. F.; Hone, J. *Proc. Natl. Acad. Sci.* **2009**, *106*, 7304-8.

(12)   Berciaud, S.; Ryu, S.; Brus, L. E.; Heinz, T. F. *Nano Letters* **2009**, *9*, 346-52.

(13)   Chan, J.; Venugopal, A.; Pirkle, A.; McDonnell, S.; Hinojos, D.; Magnuson, C. W.; Ruoff, R. S.; Colombo, L.; Wallace, R. M.; Vogel, E. *ACS nano* **2012**.

(14)   Ni, Z.; Wang, Y.; Yu, T.; You, Y.; Shen, Z. *Physical Review B* **2008**, *77*, 113407.

(15)   Yan, J.; Zhang, Y.; Kim, P.; Pinczuk, A. *Physical Review Letters* **2007**, *98*, 166802.

(16)   Shim, J.; Lui, C. H.; Ko, T. Y.; Yu, Y.-J.; Kim, P.; Heinz, T.; Ryu, S. *Nano Letters* **2012**, *12*, 648-654.

(17)   Li, X.; Cai, W.; An, J.; Kim, S.; Nah, J.; Yang, D.; Piner, R.; Velamakanni, A.; Jung, I.; Tutuc, E.; Banerjee, S. K.; Colombo, L.; Ruoff, R. S. *Science* **2009**, *324*, 1312-4.

(18)   Huang, P. Y.; Ruiz-Vargas, C. S.; van der Zande, A. M.; Whitney, W. S.; Levendorf, M. P.; Kevek, J. W.; Garg, S.; Alden, J. S.; Hustedt, C. J.; Zhu, Y.; Park, J.; McEuen, P. L.; Muller, D. A. *Nature* **2011**, *469*, 389-92.